THE O_2/N_2 RATIO AND CO_2 AIRBORNE SOUTHERN OCEAN STUDY

Britton B. Stephens, Matthew C. Long, Ralph F. Keeling, Eric A. Kort, Colm Sweeney, Eric C. Apel, Elliot L. Atlas, Stuart Beaton, Jonathan D. Bent, Nicola J. Blake, James F. Bresch, Joanna Casey, Bruce C. Daube, Minghui Diao, Ernesto Diaz, Heidi Dierssen, Valeria Donets, Bo-Cai Gao, Michelle Gierach, Robert Green, Justin Haag, Matthew Hayman, Alan J. Hills, Martín S. Hoecker-Martínez, Shawn B. Honomichl, Rebecca S. Hornbrook, Jorgen B. Jensen, Rong-Rong Li, Ian McCubbin, Kathryn McKain, Eric J. Morgan, Scott Nolte, Jordan G. Powers, Bryan Rainwater, Kaylan Randolph, Mike Reeves, Sue M. Schauffler, Katherine Smith, Mackenzie Smith, Jeff Stith, Gregory Stossmeister, Darin W. Toohey, and Andrew S. Watt

A recent Southern Ocean airborne campaign collected continuous, discrete, and remote sensing measurements to investigate biogeochemical and physical processes driving air–sea exchange of CO_2, O_2, and reactive biogenic gases.

As the primary conduit for CO_2 and heat exchange between the atmosphere and the deep ocean, the Southern Ocean is an important part of the climate system. Approximately 40% of the ocean's inventory of anthropogenic carbon entered through the air–sea interface south of 40°S (Khatiwala et al. 2009), and the region will continue to serve as an important carbon sink into the future (Ito et al. 2015). Despite its importance, the processes controlling air–sea gas exchange in the Southern Ocean are poorly represented by models. This was highlighted in a recent comparison of models from phase 5 of the Coupled Model Intercomparison Project (CMIP5), wherein the simulated seasonal cycles of air–sea CO_2 exchange with the Southern Ocean were widely divergent and in poor agreement with observational estimates (Anav et al. 2013; Jiang et al. 2014), suggesting possible model biases in the timing, spatial

AFFILIATIONS: Stephens, Long, Apel, Beaton, Bresch, Hayman, Hills, Honomichl, Hornbrook, Jensen, Powers, Reeves, Stith, Stossmeister, and Watt—National Center for Atmospheric Research, Boulder, Colorado; Keeling and Morgan—Scripps Institution of Oceanography, University of California, San Diego, La Jolla, California; Kort, Hoecker-Martínez, and M. Smith—University of Michigan, Ann Arbor, Michigan; Sweeney, Bent, and McKain—University of Colorado Boulder, and National Oceanic and Atmospheric Administration, Boulder, Colorado; Atlas, Donets, and Schauffler—University of Miami, Miami, Florida; Blake—University of California, Irvine, Irvine, California; Casey, Rainwater, K. Smith, and Toohey—University of Colorado Boulder, Boulder, Colorado; Daube—Harvard University, Cambridge, Massachusetts; Diao—San Jose State University, San Jose, California; Diaz, Gierach, Green, Haag, McCubbin, and Nolte—Jet Propulsion Laboratory, California Institute of Technology, Pasadena, California; Dierssen and Randolph—University of Connecticut, Groton, Connecticut; Gao and Li—Naval Research Laboratory, Washington, D.C.

CORRESPONDING AUTHOR: Britton B. Stephens, stephens@ucar.edu

The abstract for this article can be found in this issue, following the table of contents.

DOI:10.1175/BAMS-D-16-0206.1

A supplement to this article is available online (10.1175/BAMS-D-16-0206.2).

In final form 13 June 2017

distribution, and magnitude of the physical and biological flux drivers.

The current trajectory of Southern Ocean air–sea CO_2 fluxes is uncertain (Le Quéré et al. 2007; Landschutzer et al. 2015), the Southern Ocean is subject to strong decadal climate variability (e.g., Mayewski et al. 2009), and the Southern Ocean appears to be uniquely sensitive to anthropogenic temperature forcing (Gille 2008; Purkey and Johnson 2010; Hogg et al. 2015; Talley et al. 2016). By midcentury, CMIP5 models disagree by up to 70 PgC on the cumulative ocean carbon uptake since 2006 (Lovenduski and Bonan 2017), which is a sizable amount in comparison to annual emissions of around 10 PgC yr^{-1}, and hinders evaluation of how much fossil fuel can be burned in coming decades to maintain a specific temperature target. Given the Southern Ocean's important role in the global ocean carbon sink, confidence in model projections is further lacking as a result of the poor agreement on the Southern Ocean air–sea CO_2 flux seasonal cycle. We view the seasonal cycle as a natural laboratory within which to study the interactions of biology and physics that are key to future carbon–climate feedbacks. Current model divergence, particularly in summer, provided the central motivation behind the O_2/N_2 Ratio and CO_2 Airborne Southern Ocean (ORCAS) study. The core objective of ORCAS has been to use atmospheric measurements to advance our understanding of the physical and biological controls on summertime air–sea exchange of O_2 and CO_2 in the Southern Ocean (Fig. 1).

The strength of the Southern Ocean carbon sink is a delicate balance between opposing processes. The deep ocean is biologically enriched in natural CO_2; these waters surface in the Southern Ocean, driving natural outgassing that offsets uptake of anthropogenic CO_2. On the seasonal time scale, there is opposition between thermal and biological drivers of CO_2 flux. Warming in summer reduces CO_2 solubility, driving outgassing; however, warming is coincident with large phytoplankton blooms, driving a tendency toward net CO_2 uptake. Simultaneous measurements of O_2 and CO_2 can provide insight into the mechanisms controlling CO_2 because O_2 fluxes are positively correlated with CO_2 for thermally driven fluxes but negatively correlated for biologically driven fluxes. Moreover, air–sea O_2 fluxes have no measurable anthropogenic component, and since O_2 is not subject to carbonate buffering, the air–sea equilibration time scale is shorter and the fluxes are larger than for CO_2. Atmospheric concentration observations have a spatial advantage

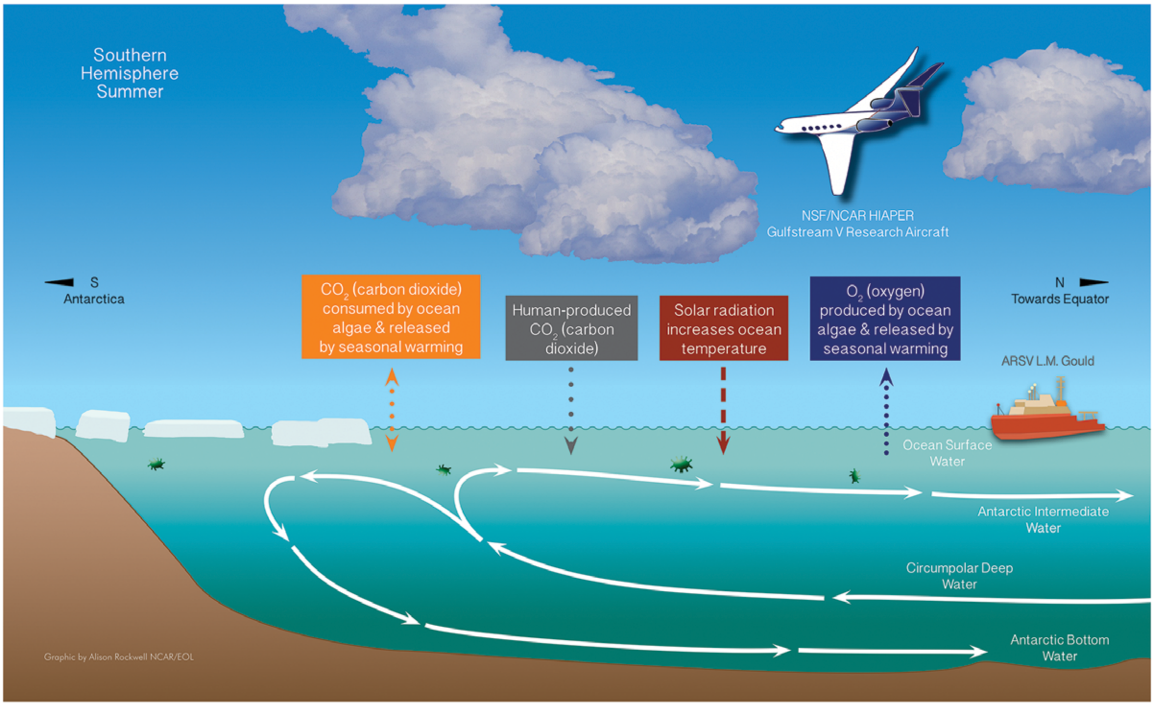

Fig. 1. Conceptual diagram of the ORCAS campaign. In summer, CO_2 is consumed by algae in the ocean surface leading to uptake, while surface warming reduces the solubility of CO_2 promoting outgassing. In contrast, algae produce O_2, which combines with surface warming, and both processes promote outgassing. By measuring both CO_2 and O_2 in the atmosphere over the Southern Ocean, we gain insights into the relative importance of thermal vs biological processes in driving air–sea CO_2 exchange. Figure courtesy of Alison Rockwell (NCAR EOL).

over hydrographic measurements, because they integrate processes over much larger areas on short time scales, thereby providing insight into behavior on regional to hemispheric scales. Airborne measurements also have advantages over air sampling from stations or ships because they can capture signals over the full tropospheric column and are less sensitive to uncertainties in atmospheric boundary layer (BL) venting.

The ORCAS campaign has produced an unprecedented, intensive set of observations in an undersampled yet vitally important part of the world. This paper presents an overview of the field campaign and initial results and describes primary research directions for potential future analyses.

ORCAS CAMPAIGN DESCRIPTION. The ORCAS campaign used the National Science Foundation/National Center for Atmospheric Research (NSF/NCAR) Gulfstream V (GV) aircraft, based out of Punta Arenas, Chile, to target a range of diverse biogeochemical regions adjacent to the southern tip of South America and the Antarctic Peninsula (Table 1;

TABLE 1. ORCAS flights during early 2016.

Flight code[a]	Date	Duration (h)	Route[b]	Objective
TF01	5 Jan	4.3	KBJC–Lamont, OK–KBJC	Instrument test flight, Total Carbon Observing Network (TCCON) comparison
TF02	7 Jan	5.5	KBJC–Gulf of Mexico–KBJC	Instrument test flight
FF01	11 Jan	9.7	KBJC–SCAR	Ferry
FF02	12 Jan	5.1	SCAR–SCCI	Ferry
RF01	15 Jan	7.7	SCCI–Marguerite Bay–SCCI	Southwest large-scale survey, remote sensing
RF02	18 Jan	7.0	SCCI–Elephant Island–SCCI	Southeast large-scale survey, marginal ice zone BL, remote sensing of Patagonian Shelf
RF03	21 Jan	8.4	SCCI–Bellingshausen Sea–SCCI	West large-scale survey, marginal ice zone, OOI node, remote sensing
RF04	23 Jan	5.7	SCCI–SCTE	Northwest large-scale survey, relocation because of high winds in SCCI
RF05	25 Jan	2.1	SCTE–SCCI	Relocation return
RF06	25 Jan	6.2	SCCI–PSA–*Gould*–SCCI	Remote sensing over Palmer Station and ship, in situ BL comparison to ship
RF07	30 Jan	7.5	SCCI–Patagonian Shelf–SCCI	Lagrangian budgeting, remote sensing of shelf
RF08	5 Feb	7.9	SCCI–Bellingshausen Sea–SCCI	Southwest large-scale survey, marginal ice zone
RF09	8 Feb	4.5	SCCI–SCTE	Northwest large-scale survey, relocation because of high winds in SCCI
RF10	10 Feb	2.0	SCTE–SCCI	Relocation return
RF11	12 Feb	8.2	SCCI–Weddell Sea–SCCI	Southeast large-scale survey
RF12	15 Feb	2.2	SCCI–SCVD	Relocation because of high winds in SCCI
RF13	17 Feb	2.2	SCVD–SCCI	Relocation return
RF14	18 Feb	7.7	SCCI–Elephant Island–Patagonian Shelf–SCCI	Southeast large-scale survey, remote sensing *Gould* track
RF15	19 Feb	2.0	SCCI–SCTE	Relocation because of high winds in SCCI
RF16	22 Feb	1.9	SCTE–SCCI	Relocation return
RF17	24 Feb	7.6	SCCI–Antarctic Peninsula–SCCI	Southwest large-scale survey, Lagrangian upwind
RF18	25 Feb	4.7	SCCI–Elephant Island–SCCI	Southeast large-scale survey, Lagrangian downwind
RF19	29 Feb	5.9	SCCI–SCAR	Northwest large-scale survey, ferry
FF03	1 Mar	9.5	SCAR–KBJC	Ferry

[a] Test flight (TF), ferry flight (FF), and research flight (RF).

[b] Broomfield, Colorado (KBJC); Arica, Chile (SCAR); Punta Arenas, Chile (SCCI); Puerto Montt, Chile (SCTE); and Valdivia, Chile (SCVD).

Fig. 2; www.eol.ucar.edu/field_projects/orcas). The GV payload included continuous sensors and whole-air samplers for O_2, CO_2, other greenhouse gases, industrial pollutants, and marine biogenic reactive gases; a hyperspectral ocean color remote sensor; and aerosol, liquid water, and cloud microphysics probes (see the "GV instrument payload" section). This payload and the performance characteristics of the GV enabled a broad set of measurement objectives over a range of spatial scales. In addition to the field component, the ORCAS project included modeling activities aimed at guiding the observational effort and providing a basis for synthesizing observations to improve our understanding of key biogeochemical processes.

Measurement objectives. The largest-scale (35°–75°S, zonal, and 0–13-km altitude) objective of the ORCAS flights was to map atmospheric O_2 and CO_2 distributions in order to characterize seasonal anomalies in these quantities associated with air–sea fluxes. Summer outgassing of O_2 and uptake of CO_2 yield a large excess of O_2 and a CO_2 deficit that are mixed throughout the troposphere; the size and temporal growth of these features provide estimates of zonally averaged fluxes over monthly to seasonal time scales (Bent 2014). By profiling frequently from the lower stratosphere to the marine boundary layer, the ORCAS flights measured vertical atmospheric O_2 and CO_2 gradients throughout the free troposphere. We targeted the O_2/CO_2 ratios of these gradients as a means to quantify the relative balance between thermal and biological forcing in driving basin-scale air–sea fluxes on time scales from weeks to months. Finally, at the regional scale, ORCAS flights included intensive boundary layer sampling between ~150 and 1,500 m, often targeting the marginal ice zone, as well as several 4–24-h Lagrangian airmass-following experiments with the objective of measuring air–sea O_2 and CO_2 fluxes over shorter temporal and spatial scales.

In addition to the primary focus on O_2 and CO_2, ORCAS included a suite of complementary research objectives, which resulted in a diverse instrument payload (Table 2). We measured the long-lived greenhouse gases and fossil fuel tracers CH_4, N_2O, and CO to investigate their potential sources and atmospheric transport to the high southern latitudes. We also measured a large number of reactive gases, many of biogenic marine origin, to characterize source regions and quantify emissions of these chemically and radiatively important species. We generated high-resolution hyperspectral ocean color images for chlorophyll and the potential for quantification of algal community composition. Finally, a full suite of cloud microphysical sensors was included on the GV, with a goal of

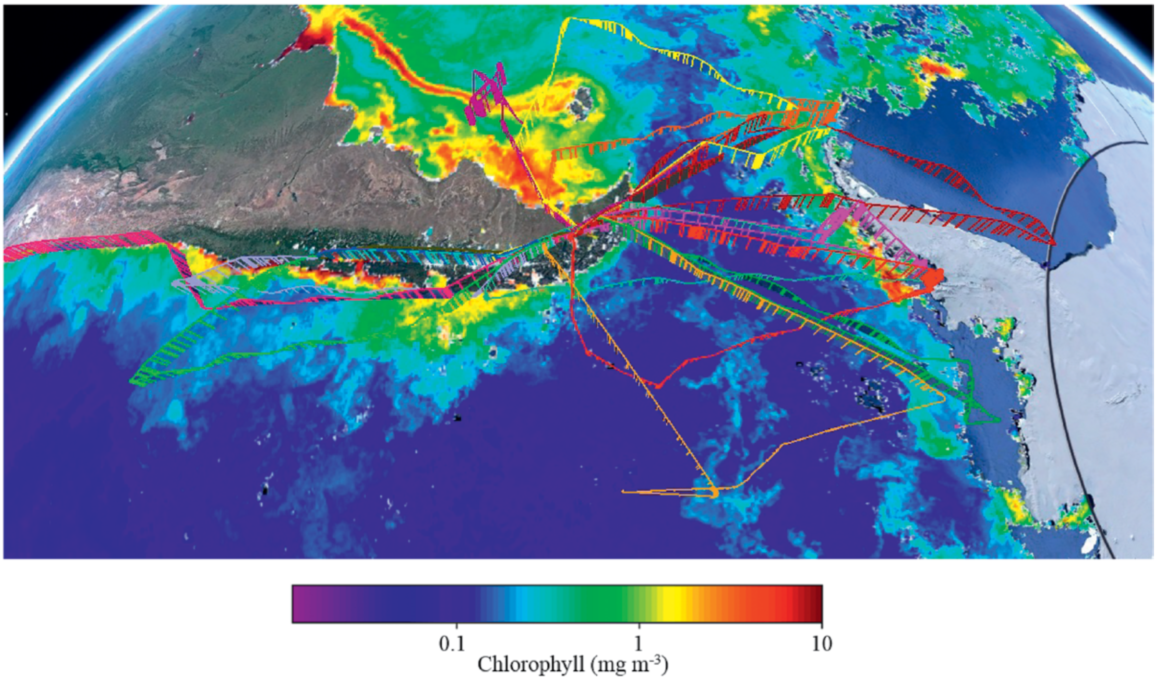

Fig. 2. ORCAS flight tracks and altitudes colored by flights. Also shown is chlorophyll a from the Visible Infrared Imaging Radiometer Suite (VIIRS) satellite instrument averaged from 17 Jan to 4 Mar. The map was produced in Google Earth, and each flight is indicated with a distinct color and vertical bars to aid visualization.

providing an observational basis for improving model representations of Southern Ocean clouds.

Analyses of the ORCAS dataset can leverage a broader set of long-term observations in the region, most notably those of the Palmer Antarctic Long-Term Ecological Research (PALTER; http://pal.lternet.edu) program, the Drake Passage time series (DPT; http://cdiac.esd.ornl.gov/ftp/oceans/VOS_Gould_Lines), and Palmer Station, Antarctica (PSA; http://scrippso2.ucsd.edu). The Antarctic Research and Supply Vessel (ARSV) *Laurence M. Gould*, which was conducting its annual PALTER cruise along the peninsula and in the Drake Passage during ORCAS, provided continuous and discrete atmospheric O_2 and CO_2 observations, as well as underway surface ocean pCO_2 and dissolved O_2 measurements (Munro et al. 2015). The ship also collected samples for algal pigments and made observations of near-surface water optical properties and hyperspectral water-leaving reflectance. Observations at PSA included flask sampling for O_2 and CO_2 by the Scripps Institution of Oceanography O_2 Program, as well as sampling for water optical properties and algal pigments at coastal station locations.

GV instrument payload. Details of the ORCAS payload are given in Table 2. The primary instrument for atmospheric O_2 measurements was the NCAR airborne oxygen instrument (AO2), which uses a vacuum ultraviolet absorption technique to make high-precision and fast-response O_2 measurements and includes a low-precision CO_2 sensor to enable dilution corrections of the O_2 signal (Stephens et al. 2003). Atmospheric O_2 measurements are reported as relative deviations in the O_2/N_2 ratio to avoid complications of dilution by other gases at the required high levels of measurement precision (Keeling et al. 1998); $\delta(O_2/N_2)$ values are multiplied by 10^6 and reported in "per meg" units. The AO2 measurements were compared to 32 whole air samples per flight, collected in 1.5-L glass flasks by the NCAR–Scripps Medusa whole-air sampler and analyzed in the Scripps O_2 Laboratory (Bent 2014). We also analyzed the Medusa flasks for CO_2, $\delta(Ar/N_2)$, and the ^{13}C and ^{18}O isotopologues of CO_2 and have preserved the CO_2 from these samples for future radiocarbon measurements. High-precision in situ measurements of CO_2 were made by two additional instruments, the Harvard quantum cascade laser spectrometer, which also made high-precision measurements of CH_4, N_2O, and CO (Santoni et al. 2014), and a National Oceanic and Atmospheric Administration–University of Colorado Boulder (NOAA–CU) Picarro G2401-m analyzer, which also made high-precision measurements of CH_4 and low-precision measurements of CO (Karion et al. 2013).

The High-Performance Instrumented Airborne Platform for Environmental Research (HIAPER) trace organic gas analyzer (TOGA) made in situ measurements of over 60 volatile organic carbon species, including dimethyl sulfide (DMS), bromoform ($CHBr_3$), and other halogenated species with distinct marine biogenic sources (Apel et al. 2015). We made additional reactive gas measurements on 56 whole-air samples per flight, collected in stainless steel canisters by the NCAR–University of Miami advanced whole air sampler (AWAS) and analyzed at the University of Miami (Andrews et al. 2016; Schauffler et al. 1999; Flocke et al. 1999).

Table 2. Instrument payload.

Instrument	Measurement	Institution
AO2	$\delta(O_2/N_2)$, CO_2	NCAR
Medusa flask sampler	$\delta(O_2/N_2)$, CO_2, $\delta(Ar/N_2)$, $\delta^{13}C$, $\delta^{18}O$, $\Delta^{14}C$ of CO_2	NCAR, Scripps
Quantum cascade laser spectrometer (QCLS)	CO_2, CH_4, N_2O, CO	Harvard, Aerodyne, NCAR, University of Michigan
Picarro G2401-m	CO_2, CH_4, CO, H_2O	NOAA, CU
HIAPER TOGA	Over 60 VOCs including OVOCs, nitriles, DMS, and halocarbons	NCAR
AWAS	Over 80 trace gases including DMS, carbonyl sulfide, halocarbons, methyl nitrate, isoprene	NCAR, University of Miami
PRISM	Hyperspectral water-leaving radiance	JPL
VCSEL, King probe, RICE, CDP, 2DC, CN, UHSAS, GNI, CLH-2[a]	Cloud microphysics, aerosol size distributions	NCAR, CU

[a] Acronyms not previously defined: Rosemount icing detector (RICE), two-dimensional optical array cloud probe (2DC), condensation nucleus counter (CN), ultrahigh sensitivity aerosol spectrometer (UHSAS), giant nuclei impactor (GNI).

In addition to gas measurement capabilities, the ORCAS payload included a remote sensing instrument: the National Aeronautics and Space Administration (NASA) Jet Propulsion Laboratory (JPL) portable remote imaging spectrometer (PRISM). PRISM imaged radiances in the near-ultraviolet to near-infrared spectral range at 10-m resolution, enabling characterization of chlorophyll and other pigments and supporting algorithm development and satellite validation (Mouroulis et al. 2014). Finally, a suite of aerosol, cloud, and precipitation probes, including a slide impactor, quantified aerosol and hydrometeor size distributions from 0.011 to 3,000 μm. Fast-response water vapor measurements were made by the vertical-cavity surface-emitting laser (VCSEL) hygrometer (Zondlo et al. 2010). Total condensed water concentrations were measured using the closed-path tunable-diode laser hygrometer (CLH-2) condensed water content probe (Dorsi et al. 2014).

Meteorology. The meteorology of the ORCAS study region during austral summer is characterized by strong midlevel westerly flow with embedded cyclones and their attendant frontal systems. The midsummer climatology exhibits a mean trough over West Antarctica and the Amundsen Sea leading to persistent, brisk westerly low-level flow over the Drake Passage with northwesterly winds farther south over the Antarctic Peninsula. These westerlies are occasionally supplanted with the circulations surrounding the transient cyclones and frontal systems moving clockwise around the climatological trough. The synoptic-scale lift provided by these transient systems along with the cool ocean surface leads to a preponderance of clouds with only occasional clear patches.

Conditions during ORCAS were generally consistent with climatological expectations in terms of strength and direction of flow, storm frequency, and atmospheric stability, with some notable deviations. In early January 2016, as the ORCAS field phase began, a strong El Niño was in progress and corresponded with a positive Antarctic Oscillation index (e.g., Thompson and Wallace 2000; Pohl et al. 2010). We examined the atmospheric climatology and anomaly patterns available from Columbia University's Climate Data Library (http://iridl.ldeo.columbia.edu/maproom/Global/Atm_Circulation/index.html) along with the National Centers for Environmental Prediction (NCEP) Global Forecast System analyses archived in the ORCAS Field Catalog (http://catalog.eol.ucar.edu/orcas) to provide the following overview of the atmospheric circulation during the campaign period. Over the study region in January, positive geopotential height and sea level pressure anomalies were found over the South Pacific between 90° and 120°W, as the climatological trough over West Antarctica was weaker and displaced farther south than normal. Negative height anomalies were centered at 30°W. These led to stronger tropospheric southwesterly flow than the climatological mean over the Drake Passage during January and a polar jet that was displaced to the south, or at times even absent, across the study region. As the height anomalies weakened beginning in late January and into February, a more zonal flow developed with more frequent cyclones moving through the Drake Passage beneath a polar jet along 60°S. During this period, sea surface temperatures were cooler than normal by 1.5–2 K from near 60°S, 100°W, across the Drake Passage, to the southern Atlantic. Conversely, there were slightly warmer-than-normal sea surface temperatures across the South Pacific, roughly aligned with the region with higher-than-normal geopotential heights and sea level pressure. The cool ocean surface resulted in minimal buoyancy forcing, and near-surface mixing was mostly the result of wind shear. Where winds were light, the atmospheric boundary layer could be quite shallow or effectively nonexistent, but surface winds were typically quite strong (10–15 m s^{-1}), and mixing was evident up to 400–1,000-m altitude on most profiles.

The rapid progression of weather systems across the study region meant that there were usually suitable sampling opportunities somewhere in the designated study region and an infrequent need to wait for better weather conditions. However, strong winds over Patagonia associated with the number of intense cyclones and frontal systems were occasionally problematic for safe crosswind takeoff and landing operations and threatened to damage the unhangared aircraft on the ground, necessitating evacuation of the aircraft from Punta Arenas on several occasions.

Flights. ORCAS included 19 research flights (RF01–RF19)—10 flights departed from and returned to Punta Arenas, conducting research over the Southern Ocean; 3 flights surveyed along the western coast of Chile; and 6 flights were for the purpose of ferrying the GV to and from a more northern location to avoid high-wind events in Punta Arenas (Table 1). In total, 98.2 research flight hours were used. Large-scale surveys were conducted to the west and east of the Drake Passage, including at the beginning (RF01, RF02, and RF03), middle (RF08 and RF11), and end (RF14, RF17, and RF18) of the campaign so as to span the full time period and establish trends. Several of these flights also targeted boundary layer sampling over the marginal ice zone, which is the biogeochemically dynamic region of partial sea ice cover and a potentially significant source of reactive gases. The most southerly sampling was done on RF11, which penetrated an Antarctic air mass over the Weddell Sea. Three flights included an explicit Lagrangian experimental design (RF07, RF17, and RF18), wherein we used simulated air parcel trajectories from an atmospheric transport model to guide our repeated sampling of an air mass as it moved over the ocean.

While the PRISM instrument operated on all the research flights, there were two dedicated remote sensing flights that targeted PRISM capabilities (RF06 and RF07) by flying in a grid pattern over a cloud-free patch of ocean. RF06 included overflights of the *Gould* south of Adelaide Island, and RF07 imaged the highly productive Patagonian shelf break. Also, during a portion of RF14, we targeted remote sensing of high-particulate inorganic carbon waters that had been sampled by the *Gould* several days earlier. Clouds were not specifically targeted in our flight plans but were intercepted multiple times on most flights, with the preponderance of these clouds at temperatures below 0°C.

To further illustrate our general approach, a video for an example flight from the forward-looking camera on the GV, along with coincident position, altitude, O_2, and CO_2 data, is provided as an electronic supplement (see page 1 of the electronic supplement at https://doi.org/10.1175/BAMS-D-16-0206.2).

MODELING TOOLS.

ORCAS used a suite of advanced weather prediction, Earth system, and atmospheric particle dispersion models to aid in mission design and flight planning. We are using these and other models to support postcampaign analysis.

AMPS. The Antarctic Mesoscale Prediction System (AMPS; Powers et al. 2012) is a real-time numerical weather prediction (NWP) system that NCAR runs in support of the U.S. Antarctic Program (USAP). The system employs the Weather Research and Forecasting (WRF) Model (Skamarock et al. 2008) for twice-daily forecasts covering Antarctica and the Southern Ocean. The model output is the basis for a wide range of forecast products that provide guidance to the weather forecasters of the USAP, whose concerns center on forecasting for the program's support flights and ground operations across the continent. The AMPS effort, however, also strives to support scientific field campaigns where possible (e.g., Powers et al. 2012), and AMPS was well positioned to provide tailored NWP for the ORCAS weather forecasters and, critically, for the missions of the GV.

For ORCAS, the AMPS team configured supplementary WRF forecast domains for the study region. An outer grid covering much of the high-latitude Southern Hemisphere with 27-km horizontal grid spacing contained a 9-km domain centered on the Drake Passage and extending from the southern Antarctic Peninsula to central Chile. These gave guidance out to 72 h via a suite of products that reflected the

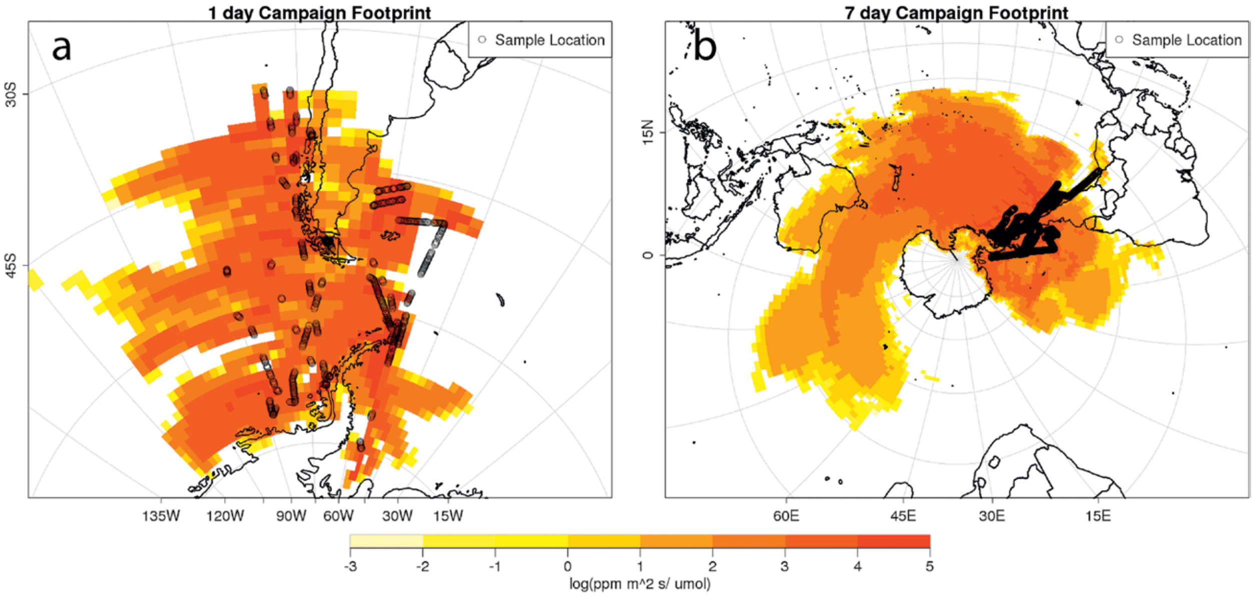

FIG. 3. STILT-generated area of surface influence (footprint) for the whole campaign using GDAS reanalysis winds and TOGA measurement locations as receptors with 4,096 particles each run backward for (a) 2 and (b) 7 days.

needs and input of the campaign forecasters and scientists. Products that were particularly useful for flight planning included storm position, turbulence, and icing conditions for flight safety, as well as boundary layer heights, clouds, and airmass histories, for targeting in situ and remote sensing legs. The WRF gridded output from the ORCAS forecasts may be obtained from the AMPS archive that resides on the NCAR High Performance Storage System (http://www2.mmm.ucar.edu/rt/amps/information/archive_info.html).

STILT. The Stochastic Time-Inverted Lagrangian Transport (STILT; Lin et al. 2003) model tracks ensembles of particle trajectories, and when run backward in time, the timing, location, and relative distribution of these particles can be used to define spatially and temporally evolving surface influence maps for each observation. ORCAS used STILT in two configurations: during the field campaign, STILT was operated in a forecast mode using winds from the Global Forecast System (GFS) 1° model (www.emc.ncep.noaa.gov/GFS/doc.php), and postcampaign, STILT was operated in a reanalysis mode using Global Data Assimilation System (GDAS) winds with 0.5° resolution (http://ready.arl.noaa.gov/gdas1.php). Both model wind fields are available from the NOAA Air Resources Laboratory in a format to be used with the Hybrid Single-Particle Lagrangian Integrated Trajectory model (HYSPLIT; Stein et al. 2015) that underlies STILT.

In forecast mode, nightly predictions were made using the 0000 UTC forecast for generic flights 1 and 2 days in the future. These trajectories gave the 48-h history and 24-h future evolution of the sampled air, using 128 particles over the previous 48 h for each of ~200 receptors per flight. A more specific draft plan was created on the day preceding a proposed flight, and trajectories were generated for that flight. Computation was rapid enough to allow for several iterations before a final flight plan was submitted to pilots and air traffic control. This rapid iteration allowed the ORCAS campaign to include a pair of flights (RF17 and RF18) where the same air mass was sampled twice on two consecutive days.

After the campaign, STILT was rerun for the flights as flown using the 0.5° GDAS reanalysis winds to estimate the times and areas of influence for the actual observations. Receptors were collocated with the ~2,000 per flight (~2 min^{-1}) sample locations of the TOGA instrument. In postanalysis, we used 4,096 particles per receptor and extended the time span of integration to 1 week. The resulting whole-campaign surface influence maps, or footprints, defined by the fraction of particles within the boundary layer, are shown in Fig. 3. These footprints indicate that over 2 days preceding the measurements, the region of air–sea flux influence on the observations was confined to the eastern South Pacific sector of the Southern Ocean. Looking 7 days back, the observations saw air–sea flux influence from the entire mid- to high-latitude South Pacific, as well as large portions of the Atlantic sector of the Southern Ocean. Influence maps for individual samples can be used to link changes in atmospheric composition to a variety of flux fields from observationally based products as well as biogeochemical model integrations. This framework can provide a means of optimizing flux estimates on the basis of the ORCAS observations.

CESM forecasts. In support of the field campaign, we developed a novel configuration of the Community Earth System Model (CESM; Hurrell et al. 2013) to

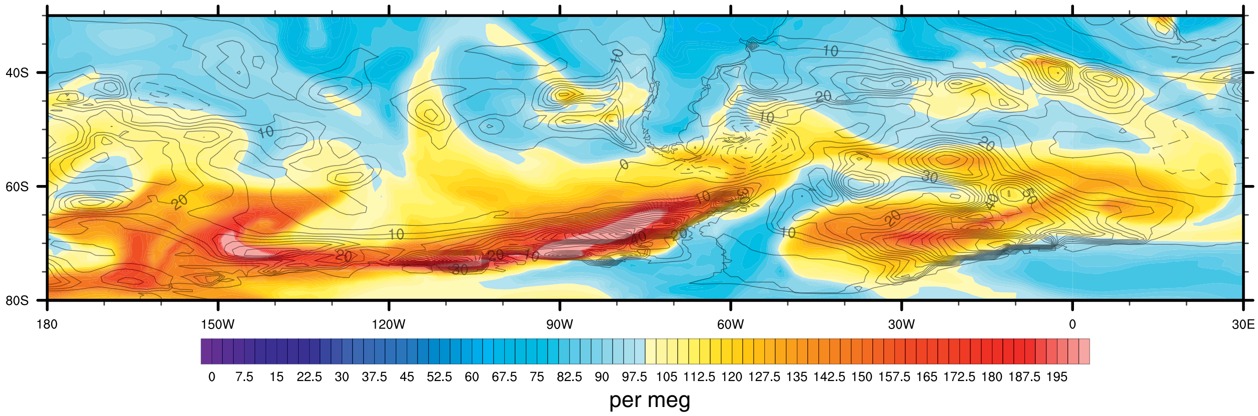

Fig. 4. Example output from the CESM biogeochemical forecast system on 18 Jan 2016, the date of RF02. Color shows the anomaly in oxygen concentration ("per meg" units) at the surface induced by air–sea exchange; contours show the sea-to-air oxygen flux (contoured from −130 to 130 mol $\text{m}^{-2}\,\text{yr}^{-1}$ with an interval of 5 mol $\text{m}^{-2}\,\text{yr}^{-1}$); dashed contours indicate negative fluxes (ocean uptake).

produce biogeochemical forecasts. This configuration consisted of a prognostic, three-dimensional ocean component [Parallel Ocean Program, version 2 (POP2)], a land surface model [Community Land Model, version 4.5 (CLM4.5)], and an atmosphere model [Community Atmosphere Model, version 5 (CAM5)]. To enable meaningful forecasts, we nudged CAM5 within the free troposphere to wind and temperature fields from the Goddard Earth Observing System, version 5 (GEOS-5), numerical weather prediction model (Rienecker et al. 2008) such that the large-scale atmospheric state and dynamics of CAM5 matched those of the initialized forecast, but surface fluxes and ocean column physics remained freely evolving. The ocean model included a biogeochemical component (Moore et al. 2013), yielding a prognostic representation of surface O_2 and CO_2 fluxes, and these constituents were transported in the atmosphere. We used this CESM configuration to generate 3-day forecasts every day during the field campaign.

The CESM forecasts were extraordinarily helpful for flight planning and hypothesis development. One major advantage was the ability to visualize large-scale patterns and the impact of transport on tracer fields. For instance, Fig. 4 shows example output corresponding to RF02 near the beginning of the campaign. During this time, the model showed strong outgassing of O_2 along the western Antarctic margin; the oxygen plume generated by this feature was transported east, leading to a filament of high atmospheric concentrations in Drake Passage—where local sea-to-air fluxes were much weaker. A second valuable aspect of the model solution was its ability to track the evolution of the system over time, informing us of seasonal transitions. The CESM framework continues to be useful postcampaign, providing a self-consistent system to compare with observations and enabling hypothesis testing and validation. An animation of CESM simulated oceanic O_2 and CO_2 atmospheric tracers is included as an electronic supplement (see page 2 of the electronic supplement at https://doi.org/10.1175/BAMS-D-16-0206.2).

OXYGEN AND CARBON DIOXIDE. During ORCAS, we measured distinct atmospheric signals reflecting Southern Ocean outgassing of O_2 and uptake

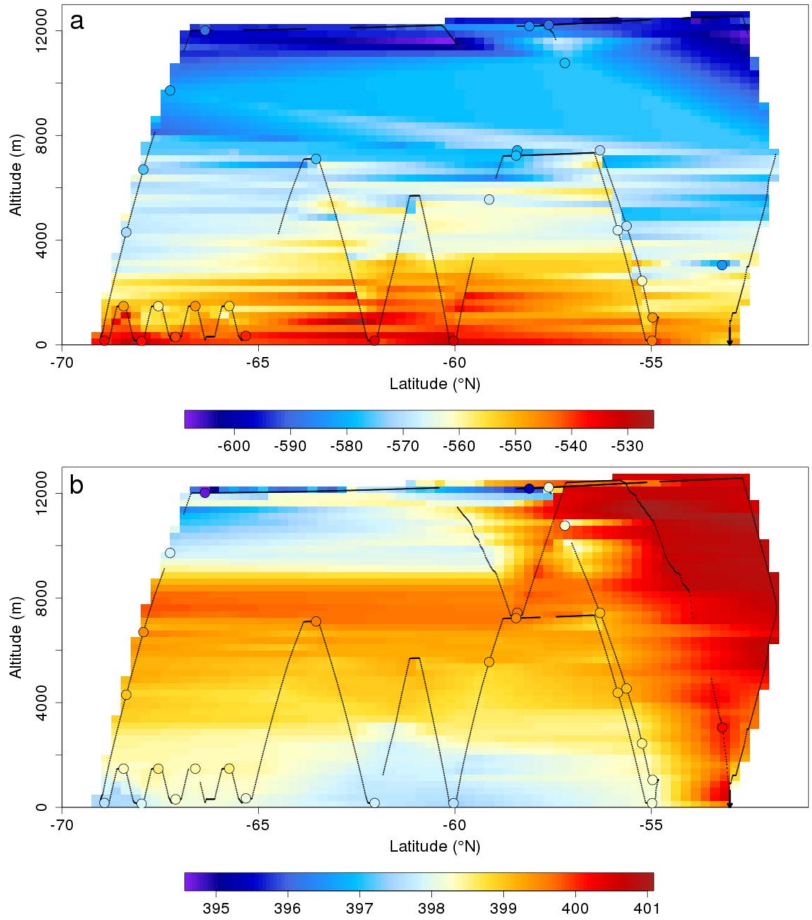

FIG. 5. Interpolated cross sections from RF03 for (a) $\delta(O_2/N_2)$ (per meg) on the Scripps O_2 scale and (b) CO_2 (ppm). The locations of the in situ measurements along the flight track are shown as small black dots, while measurements on Medusa flask samples are shown as colored circles. Contouring was done using bicubic spline interpolation with the Akima package in R (Akima 1978). Vertical arrows indicate the location of takeoff and landing. The in situ O_2 is from the AO2 instrument, while in situ CO_2 is from the NOAA–CU Picarro instrument. Gaps in the CO_2 trace correspond to times when the instrument was calibrating. Gaps in the O_2 trace correspond to instrument calibrations and filtering data between 200 and 400 hPa at airspeeds >215 m s^{-1} when the AO2 inlet fractionated air. The N_2O measurements from QCLS indicate that the profiles north of 55°S were fully in the troposphere and that the tropopause was at 7.5–8 km south of 58°S. Satellite observations showed the marginal ice zone between 67.5° and 69°S along the flight track.

of CO_2. Cross sections for these gases from a typical flight (RF03) are shown in Fig. 5; this flight originated in Punta Arenas, flew to the Bellingshausen Sea marginal ice zone, and then profiled northward along 90°W. The O_2/N_2 ratio was enhanced at low altitudes over a broad latitudinal range from 59° to 70°S, by 30 per meg, roughly equivalent to 6 ppm of O_2. In a near mirror image of this, we observed widespread low-level CO_2 depletions of approximately 1.5 ppm. Within the atmospheric boundary layer, we observed O_2 enhancements as large as 50 per meg and CO_2 depletions as large as 2 ppm, with the greatest signals on this flight coincident with the marginal ice zone (Fig. 5).

On RF03 and other flights, midtroposphere O_2 was enhanced with respect to air at higher altitudes and lower latitudes, reflecting the accumulated outgassing over the previous few months driven in part by summertime net community production in the surface ocean. Stratospheric air is relatively isolated from direct surface influences and thus responds with temporal lags as signals mix across the tropopause. The lower stratosphere had O_2 concentrations less than those of the midtroposphere. Since atmospheric O_2 is steadily declining because of fossil fuel burning, we expect higher O_2 in the older air masses aloft; thus, we infer that the O_2 gradient across the tropopause at high southern latitudes may be strongly influenced by seasonal fluxes. In contrast to O_2, the amplitude of seasonal changes in CO_2 at high southern latitudes is small relative to the annual growth rate: the ratio of peak-to-peak seasonal amplitudes to the annual trend is 5 for O_2 but only 0.6 for CO_2 (http://scrippso2.ucsd.edu). This is consistent with the observed shift to lower CO_2 in the high-latitude lower stratosphere, positively correlated with the O_2 shift, and reflecting a lag relative to the steady upward march of tropospheric CO_2 (Fig. 5). Another distinct feature in high-altitude CO_2 was the penetration of upper-tropospheric air with elevated CO_2 from the north (see "Methane and carbon dioxide" section).

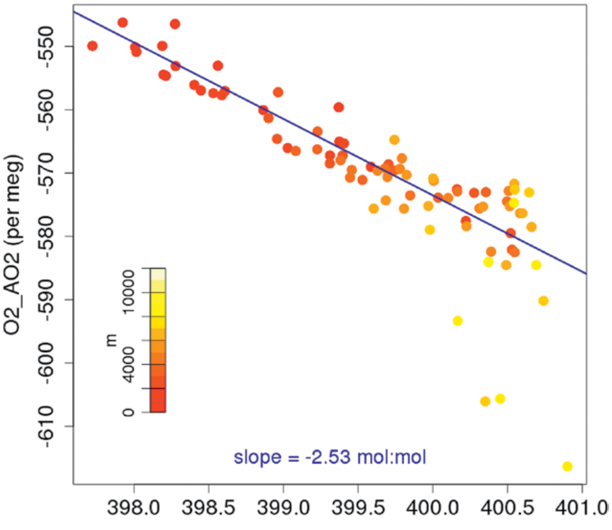

Fig. 6. Whole-campaign tropospheric relationship between O_2 and CO_2. Points were obtained by binning all data from 30° to 75°S by 5° of latitude and 1,000-m altitude and then averaging. Stratospheric points are excluded with a criterion of bin-average N_2O values <326 ppb. Points are colored by altitude. Line and reported slope are from a fit to all points below 8,000 m using orthogonal distance regression and assuming errors in O_2 and CO_2 are equivalent on a molar basis.

Figure 6 shows O_2 versus CO_2 observations for the entire campaign, averaged in 5°-latitude by 1,000-m-altitude bins. The upper-tropospheric values diverge because of the temporal factors described above, but from the ocean surface to 8 km, we found a tight O_2–CO_2 correlation with a slope corresponding to –2.5 moles of O_2 per mole of CO_2. This ratio does not correspond to that of any particular ocean process but rather emerges from combined influences. Photosynthesis in the ocean mixed layer produces O_2 and consumes CO_2 with a ratio of about –1.45 (Anderson and Sarmiento 1994). As the summer bloom begins, therefore, we expect a negative relationship between O_2 and CO_2 fluxes. However, carbonate buffering chemistry prolongs the CO_2 equilibration time scale to several months versus a few weeks for O_2; thus, mixed-layer O_2 concentrations are restored to equilibrium more quickly, shutting off O_2 gas exchange, while mixed-layer CO_2 deficits persist. This pattern leads us to expect air–sea flux ratios that are initially strongly negative but diminish in magnitude and approach zero as the season progresses. Summertime surface warming drives tendencies that are superimposed on these biological processes: warming will enhance O_2 outgassing while countering the CO_2 ingassing. Again, given the differing equilibration time scales, this should enhance the negative O_2/CO_2 flux ratios induced by biology since the O_2 flux will respond more strongly; purely thermal forcing, by contrast, would drive positive flux ratios. Given these distinct forcings and time scales, it is quite remarkable that the campaign-mean O_2/CO_2 correlation is so tight and the ratio fairly consistent from the surface through the upper troposphere. The negative slope of this relationship is indicative of the dominance of biological versus thermal forcing driving summertime fluxes. Moreover, it appears that the atmosphere acts as an efficient integrator of short-term and local air–sea fluxes, when averaging over 6 weeks and 98 h of flights.

The net O_2 outgassing and CO_2 uptake is reflected in O_2 accumulation and CO_2 drawdown in the lower troposphere averaged over the whole campaign (Fig. 7). Relative to values in the midtroposphere (4–6 km), the ORCAS observations suggest an O_2 excess of 20 per meg and CO_2 deficit of ~1.5 ppm below 1 km. We hypothesize that the strength of these vertical gradients, averaged over the 6-week campaign, largely reflect the magnitude of zonally integrated fluxes. Our CESM forecast model reproduces similar structure in O_2 and CO_2 (blue lines; Fig. 7). The tight agreement between the CESM campaign mean CO_2 profile and the ORCAS observations is striking (Fig. 7b) but possibly fortuitous. The CESM forecast model overestimated the campaign mean O_2 gradients below 4 km by approximately 50% (Fig. 7c), suggesting that the balance of processes resulting in the simulated CO_2 gradient is not consistent with the observations. Overestimation of only the O_2 gradients might result from positive biases in both the thermal and biological forcing; such errors will compensate for CO_2 but reinforce for O_2. This scenario might arise in a number of ways. Too few clouds or too little sea ice in the model might result in too much solar radiation penetrating to the ocean surface, leading to more surface warming than is appropriate and possibly fueling higher rates of productivity. Excessive summertime surface heating is consistent with ocean mixed layers that are too shallow—and indeed, most models contributing to the CMIP5 experiments, including CESM, have shallow summertime mixed-layer depth biases (Downes et al. 2015). However, primary production in the Southern Ocean surface tends to be strongly iron limited; since vertical exchange is the dominant source of iron to the mixed layer (Tagliabue et al. 2014), the greater stratification implied by shallower mixed-layer depths should be associated with diminished iron supply—which is not consistent with greater productivity. More work is required to understand these results; however, it is clear that O_2 and CO_2 provide a more powerful constraint together than either gas does alone, possibly enabling better evaluation of divergent Earth system model simulations (Anav et al. 2013; Jiang et al. 2014).

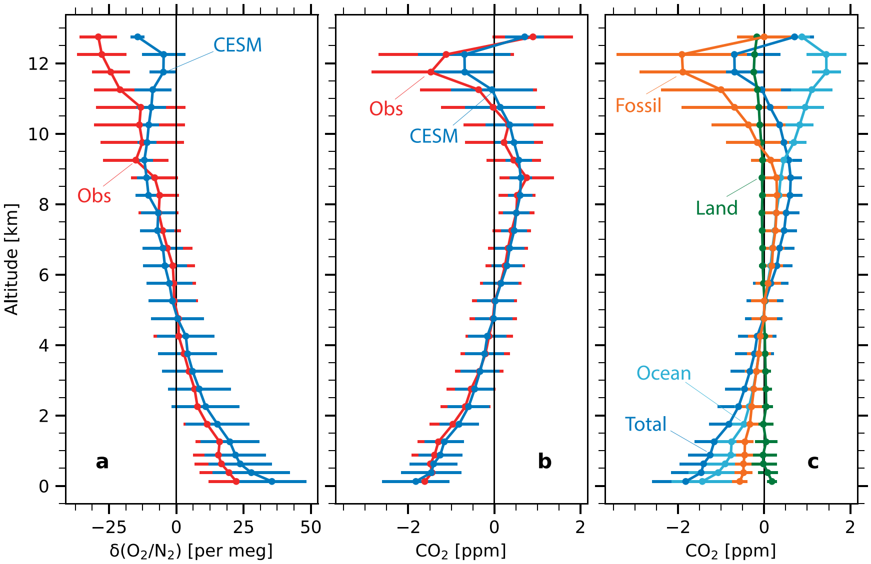

Fig. 7. Normalized, altitude-bin-averaged vertical profiles of observed (red) and simulated (blue) (a) $\delta(O_2/N_2)$, (b) CO_2, and (c) CO_2-component tracers, including total [blue; reproduced from (b)], ocean (light blue; O_2^{ocn}), land (green; CO_2^{lnd}), and fossil fuel (orange; CO_2^{ff}). Profiles are normalized by subtracting the 4–6-km mean to illuminate the vertical structure. Error bars show the standard deviation of data in each altitude bin. Simulated constituents are interpolated to the location of the observations using daily mean output from CESM runs described in the text, which include nudging to GEOS-5. Simulated $\delta(O_2/N_2)$ is derived from an oceanic oxygen tracer combined with land and fossil fuel influences on oxygen using the formula described in Stephens et al. (1998): $\delta(O_2/N_2)^{CESM} = O_2^{ocn}/\chi_{O_2} - 1.1CO_2^{lnd}/\chi_{O_2} - 1.4\,CO_2^{ff}/\chi_{O_2} - N_2^{ocn}/\chi_{N_2}$, where $\chi_{O_2} = 0.2095$ and $\chi_{N_2} = 0.7808$ are the mixing ratios of O_2 and N_2, respectively, and N_2^{ocn} is an abiotic N_2 tracer defined in CESM.

An additional complexity involved with interpreting the vertical structure in the CO_2 profile is the confounding influence of fossil fuel emissions and terrestrial fluxes. CESM suggests that fossil fuel emissions, largely in the Northern Hemisphere, contribute about 0.5 ppm to the CO_2 gradient for the campaign average below 5 km (Fig. 7c), which equates to about 3 per meg in the O_2 gradient using –1.4 as the average O_2/CO_2 combustion ratio (Steinbach et al. 2011). The model suggests that fluxes from land impart very little vertical structure to the CO_2 profile, indicating that the ORCAS measurements are largely reflective of Southern Ocean influences (light blue; Fig. 7c). The CO_2 emissions used in CESM are based on datasets with relatively robust constraints at the hemispheric scale, which is relevant to understanding impacts to the vertical profile of CO_2 over the Southern Ocean. The land fluxes, by contrast, are prognostic and could have dramatic biases. The extent to which these might impact the vertical CO_2 profile is mitigated by the fact that the Southern Ocean is remote, and thus, gradients induced by land fluxes are likely to dissipate. It may be possible to exploit the multiple industrial tracer observations from ORCAS to empirically estimate more northern influences on CO_2 and O_2. We are also engaged in analyzing the spatial and temporal evolution in the ratio of O_2 and CO_2 vertical gradients across the top of the atmospheric boundary layer, using atmospheric mass balances to estimate seasonal net outgassing of O_2, comparing vertical CO_2 distributions to climatological flux–based estimates, and making direct air–sea O_2 and CO_2 flux estimates using STILT.

METHANE AND CARBON DIOXIDE. While CO_2 gradients across the top of the atmospheric boundary layer related to ocean uptake were observed throughout the campaign, gradients of CO_2 and CH_4 across the full altitude and latitude range covered by the campaign (Fig. 8) reflected larger-scale patterns of transport and aging with virtually no local sources of CH_4 and anthropogenic CO_2. At altitude, a tongue of high-CO_2 and high-CH_4 air intruded into the domain from the north. This region also had relatively higher concentrations of CO and other pollutants ("Volatile organic compounds" section), consistent with long-range transport of air influenced by more northern terrestrial emissions.

Regions of high zonal wind speeds were observed above ~7-km altitude (Fig. 8c) and between 70° and 40°S, corresponding with the meandering jet. The position of the jet appears to delineate a transport boundary where CO_2 and CH_4 were enhanced to the north of 55°S, while aged air depleted in CO_2 and CH_4 was observed above ~9 km and south of 55°S. The isolation of polar tropospheric air is evidenced in the constancy and homogeneity of the observed CH_4 concentrations ($1\sigma = 3$ ppb on 1-s data) for the duration (46 days) of the campaign at potential temperatures <305 K.

In tracer–tracer space (Fig. 8d), polar-cell air was characterized by a vertical tail of concurrent depleted CO_2 and stable CH_4. This portion of the CH_4 dataset is characterized by intraflight variability of 1 ppb (1σ), with the rest of the variability driven by consistent flight-to-flight decreases, as concentrations approached the seasonal minimum in March. This spatial homogeneity and temporal consistency indicates that chemical destruction was the dominant process controlling CH_4 levels, with very little evidence of input by emissions or long-range transport into the Southern Ocean region. In future analyses, we aim to characterize the mixing and residence time of polar-cell air and quantify input by long-range transport using both transport models and simple chemistry models for CH_4 and other measured tracers with a chemical oxidation sink.

VOLATILE ORGANIC COMPOUNDS. TOGA and AWAS provided measurements of many volatile organic compounds (VOCs), including nonmethane hydrocarbons (NMHCs), halogenated volatile organic compounds (HVOCs), oxygenated VOCs (OVOCs), alkyl nitrates, nitriles, and

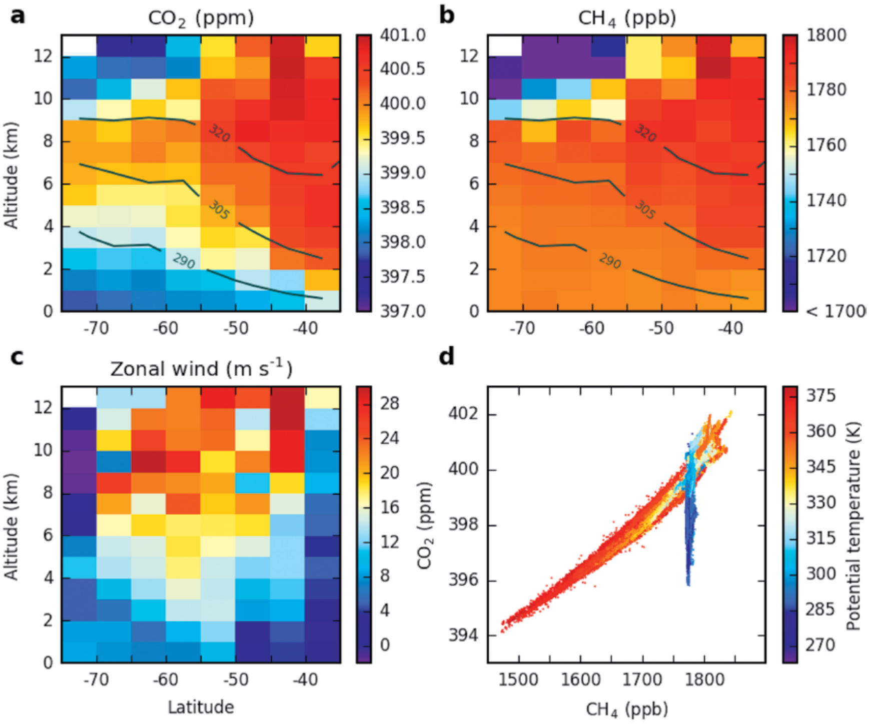

Fig. 8. Whole-campaign cross sections of (a) CO_2, (b) CH_4, and (c) zonal wind speed, averaged by 5°-latitude and 1,000-m-altitude bins, with contours of potential temperature (K) in (a) and (b). (d) Measured CO_2 vs CH_4 colored by potential temperature (K) from the full campaign dataset, aligned in 1-s time bins. The CO_2 and CH_4 measurements are from the NOAA–CU Picarro instrument.

dimethyl sulfide (DMS). Mixing ratios of VOCs with known continental sources observed during ORCAS were very low in comparison to measurements made over the tropical and midlatitude Pacific Ocean using the same instrumentation during previous January and February field campaigns, Tropical Ocean Troposphere Exchange of Reactive Halogen Species and Oxygenated VOC (TORERO; Volkamer et al. 2015) and Convective Transport of Active Species in the Tropics (CONTRAST; Pan et al. 2016; Fig. 9). The distributions of dichloromethane (CH_2Cl_2) and chloroform ($CHCl_3$) showed large north–south asymmetries that reflected stronger anthropogenic sources in the Northern Hemisphere. Dichloromethane revealed cross-hemispheric transport in the upper troposphere, with elevated mixing ratios aloft over the Southern Ocean and no apparent ocean sink. This is consistent with what is known about dichloromethane sources. Industry is believed to be responsible for the majority of dichloromethane emissions (Simmonds et al. 2006; Montzka et al. 2011), with only 1% of these emissions originating in the Southern Hemisphere (McCulloch et al. 1999). Biomass-burning emissions are more uncertain

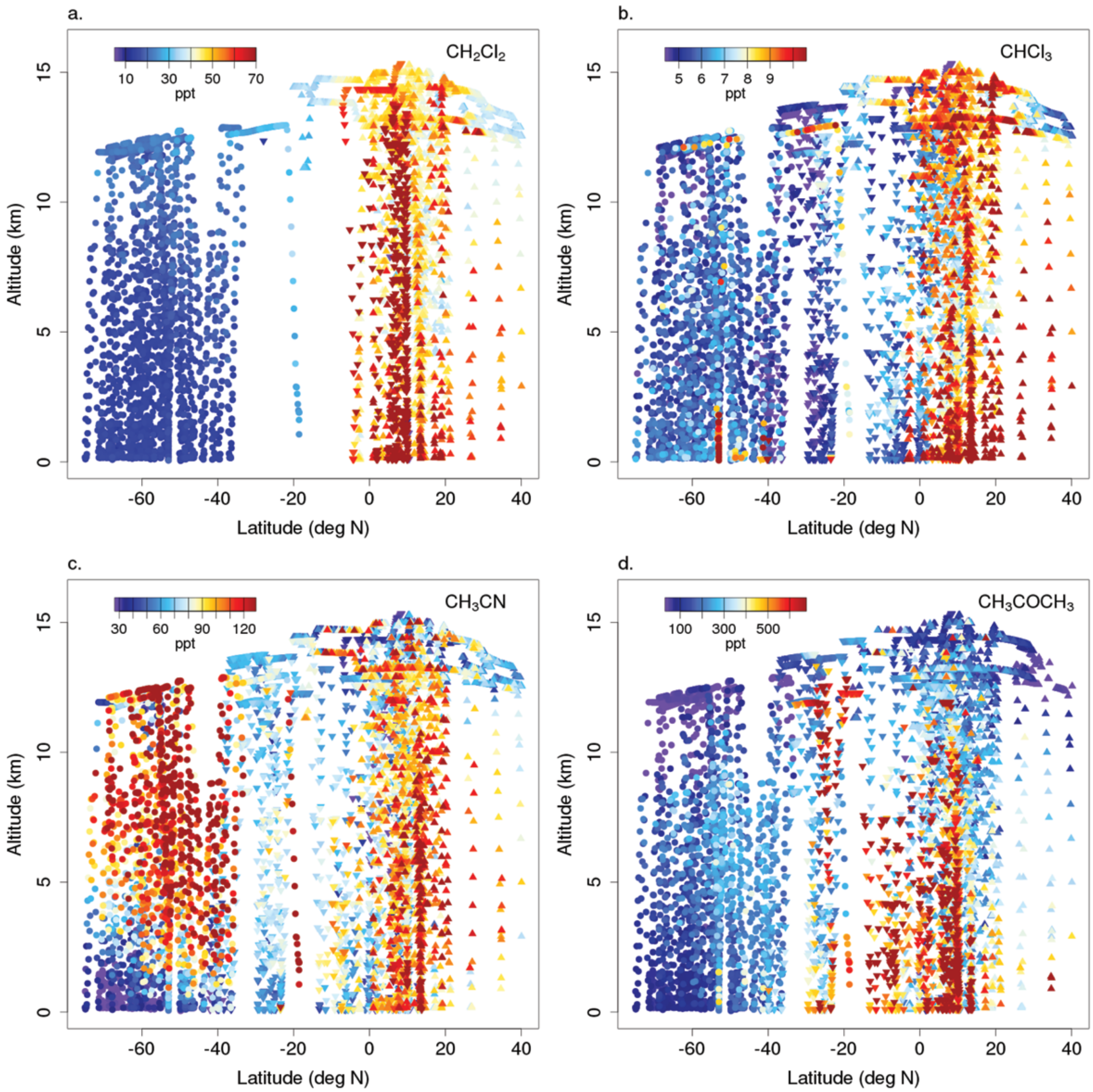

Fig. 9. Altitude vs latitude plots colored by VOC mixing ratio of (a) dichloromethane (CH_2Cl_2), (b) chloroform ($CHCl_3$), (c) acetonitrile (CH_3CN), and (d) acetone (CH_3COCH_3) from TOGA observations over the Pacific Ocean in Jan and Feb during ORCAS (circles; 2016), CONTRAST (triangles; 2014), and TORERO (inverted triangles; 2012). Values outside the color-scale ranges are plotted as the extreme colors. Symbols are plotted in order of concentration such that higher-concentration points overlay lower-concentration points.

but are estimated to be on the order of 10% of the industrial emissions (Keene et al. 1999; Montzka et al. 2011). The emission inventory for chloroform is much less certain (Montzka et al. 2011) but the Northern Hemisphere is believed to provide the majority of the emissions for this gas as well. The lifetimes of dichloromethane and chloroform, ~5 and ~6 months, respectively (Montzka et al. 2011; Khalil and Rasmussen 1999), are approximately half the interhemispheric transit time between the Northern and Southern Hemispheres (Holzer and Waugh 2015), allowing inferences developed using these and other reactive tracers to inform our understanding of the global O_2 and CO_2 interhemispheric transport.

The ORCAS dataset provides some of the first observations of Southern Hemisphere distributions of two of the most abundant nonmethane VOCs in the atmosphere: acetone (CH_3COCH_3) and acetonitrile (CH_3CN; Fig. 9). The ocean plays a significant but still uncertain role in the global acetone budget (e.g., Singh et al. 2003; Marandino et al. 2005) with our present understanding (Fischer et al. 2012) evolving to view the ocean as a net source or sink depending on the atmospheric acetone concentration and the air and seawater temperature. The ocean's role as a sink for acetonitrile is not well understood (e.g., de Gouw et al. 2003). Within the broader perspective provided by TORERO and CONTRAST, the observations in

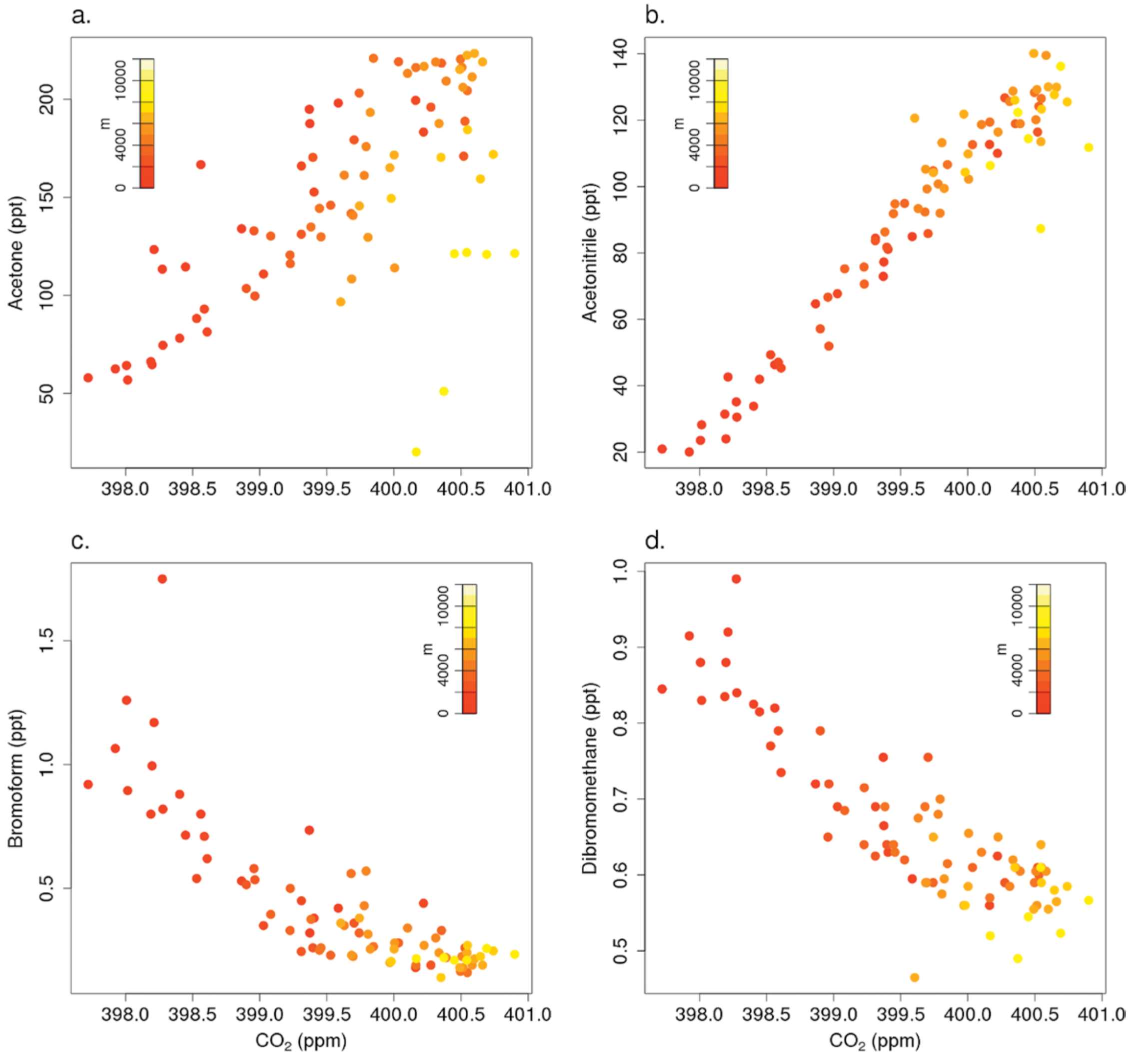

Fig. 10. Selected tropospheric VOC data observed by TOGA and AWAS during all ORCAS flights, binned by 1,000-m altitude and 5° latitude and plotted vs CO_2 data averaged over the time scale of the respective VOC measurement and similarly bin averaged. Stratospheric points are excluded with a criterion of binned N_2O values <326 ppb. Points are colored by altitude. (a) Acetone (CH_3COCH_3) and (b) acetonitrile (CH_3CN) were measured by TOGA, and (c) bromoform ($CHBr_3$) and (d) dibromomethane (CH_2Br_2) were measured by AWAS.

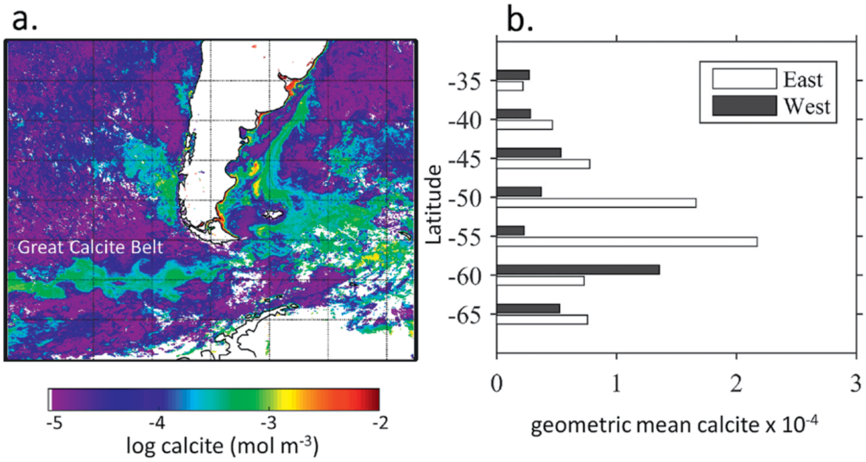

Fig. 11. Particulate inorganic carbon or calcite estimated from the Moderate Resolution Imaging Spectroradiometer (MODIS) *Aqua* sensor during ORCAS. Evident are the presence of the Great Calcite Belt and the large differences between the Pacific (west) and Atlantic (east) sectors.

Fig. 9 show clear signs of depleted concentrations for both of these species at low altitudes over the Southern Ocean, reflecting uptake, and enabling further testing of our understanding of the role that the ocean plays in the global distribution of these species.

Figure 10 shows a subset of the ORCAS TOGA and AWAS observations plotted versus CO_2 concentration. The vertical distributions of acetone and acetonitrile (Figs. 10a,b) show lower mixing ratios in low-altitude air, coincident with lower CO_2 and consistent with ocean uptake. In contrast, the ocean is known to be a primary source for bromoform ($CHBr_3$) and dibromomethane (CH_2Br_2; e.g., Goodwin et al. 1997), species that have a large impact on natural stratospheric ozone destruction, and DMS, an important precursor for natural aerosol formation in marine environments (Andreae and Crutzen 1997). Figures 10c and 10d show that bromoform and dibromomethane were anticorrelated with CO_2 in the ORCAS domain at mid- to low altitudes, reflecting ocean outgassing. The relationships between reactive gases, O_2, and CO_2 observed during ORCAS will provide insights into potential biological or gas exchange mediation of these sink or source processes, and we also plan direct flux estimation of reactive gases using STILT footprints.

SATELLITE AND AIRCRAFT REMOTE SENSING OF OCEAN COLOR.

Spectral measurements of the ocean from both satellite and aircraft data provide estimates of phytoplankton abundance and composition, as well as indications of other biogeochemically relevant quantities such as calcium carbonate. Satellite remote sensing can provide relatively accurate concentration estimates of chlorophyll a, the primary light-absorbing pigment in all phytoplankton, over kilometer spatial scales. Satellite observations were used to monitor changes in surface chlorophyll and, through application of empirical algorithms, net primary productivity (NPP) over the duration of the ORCAS experiment (Fig. 2). In addition to NPP, air–sea CO_2 flux is sensitive to the rate of calcium carbonate ($CaCO_3$) production, which consumes alkalinity, thereby raising surface ocean pCO_2. Coccolithophores are the dominant algal taxon producing $CaCO_3$ in the Southern Ocean, and their prevalence can be monitored by ocean color satellites. Indeed, the ORCAS study region encompasses a feature known as the "Great Calcite Belt" (Balch et al. 2011), where satellite observations indicate that coccolithophore abundance is particularly high (Fig. 11).

Hyperspectral remote sensing provides more than just chlorophyll-a concentrations; since phytoplankton produce numerous other pigments, each taxon can have a unique spectral "fingerprint." Ongoing research aims to calibrate spectral observations to enable quantification of phytoplankton community composition via remote sensing. In collaboration with the PALTER program, ship-based measurements of hyperspectral optical properties and phytoplankton composition were taken aboard the *Gould* coincident with the ORCAS field campaign to provide the foundations for inversion modeling of phytoplankton composition. A PRISM overflight near Palmer Station revealed localized bloom dynamics (Fig. 12); previous studies have attributed similar features to glacial meltwater, sea ice, and other environmental forces (Dierssen et al. 2002). Within ORCAS, the local-scale remotely sensed phytoplankton abundance and taxonomy from PRISM can provide a basis for testing model skill in conjunction with the broader-scale insights from in situ O_2 and CO_2 observations. PRISM-derived phytoplankton taxonomy can additionally improve species-specific understanding of reactive trace gas production by marine biota.

CLOUD MICROPHYSICS.

The ORCAS flight profiles frequently encountered clouds, enabling robust sampling of both warm marine boundary layer and cold upper-tropospheric cloud properties. Clouds over the Southern Ocean are not well treated in reanalysis and coupled climate models (Trenberth and Fasullo 2010); the models underestimate cloud amounts, thereby allowing too much solar radiation to enter the ocean. By analysis of 34 CMIP5 historical runs, Ceppi et al. (2012) suggested that biases in midlatitude cloud radiative forcings were likely caused by errors in cloud fraction or optical depth over the entire midlatitudes. Changes in cloud properties may affect the locations of jet streams over the Southern Hemisphere (Ceppi et al. 2014), and Naud et al. (2012) suggested that a lack of modeled cloudiness in the Southern Hemisphere may in part be due to the models having too few clouds in Southern Hemisphere fronts. Contributing factors to uncertainty in simulating Southern Ocean clouds include, for example, concentrations of cloud condensation nuclei (CCN) and their origin from either anthropogenic or natural sources, as well as the degree of supersaturation experienced in clouds.

The ORCAS measurements of cloud droplet size distributions in the marine boundary layer offer a new dataset on cloud properties, their formation conditions, and the relationship to natural and anthropogenic air masses. Some studies have suggested that marine boundary layer clouds over the Southern Ocean are formed in very clean air masses, with few CCN (e.g., Boers et al. 1996). This should lead to clouds with relatively few but large drops under normal conditions. Figure 13 shows the measured cloud droplet concentration for 4,421 cloudy seconds as observed using the cloud droplet probe (CDP; 1–25-μm radius range; Droplet Measurement Technologies) from the GV during ORCAS. These measurements show a broad range of cloud droplet concentration N_c with an average value of 84 cm^{-3}, which is roughly in line with typical satellite values. However, this concentration as obtained in the ORCAS flight region (clouds observed from 36° to 71°S) is 44% lower than the mean value observed by similar measurements (~150 cm^{-3}) from the NSF/NCAR C-130 taken during the 2008 Variability of American Monsoon Systems (VAMOS) Ocean–Cloud–Atmosphere–Land Study (VOCALS) marine stratocumulus deployment over the southeastern Pacific west of northern Chile; see project description in Wood et al. (2011). Thus, the measurements obtained during ORCAS point to a lower mean droplet concentration. Nonetheless, ORCAS did sample clouds at high latitudes with droplet concentrations as high as 300–400 cm^{-3} at times. It is not clear if these high drop concentrations are caused by anthropogenic aerosol contribution to the ORCAS study region or if sea-spray generation under conditions of high wind speeds led to the occasional high drop concentrations, as suggested by Chubb et al. (2016) for other measurements taken south of Australia. In the future, we will use the STILT backward particle modeling framework to facilitate understanding of the airmass histories and origins of differing cloud droplet concentrations over the ORCAS domain.

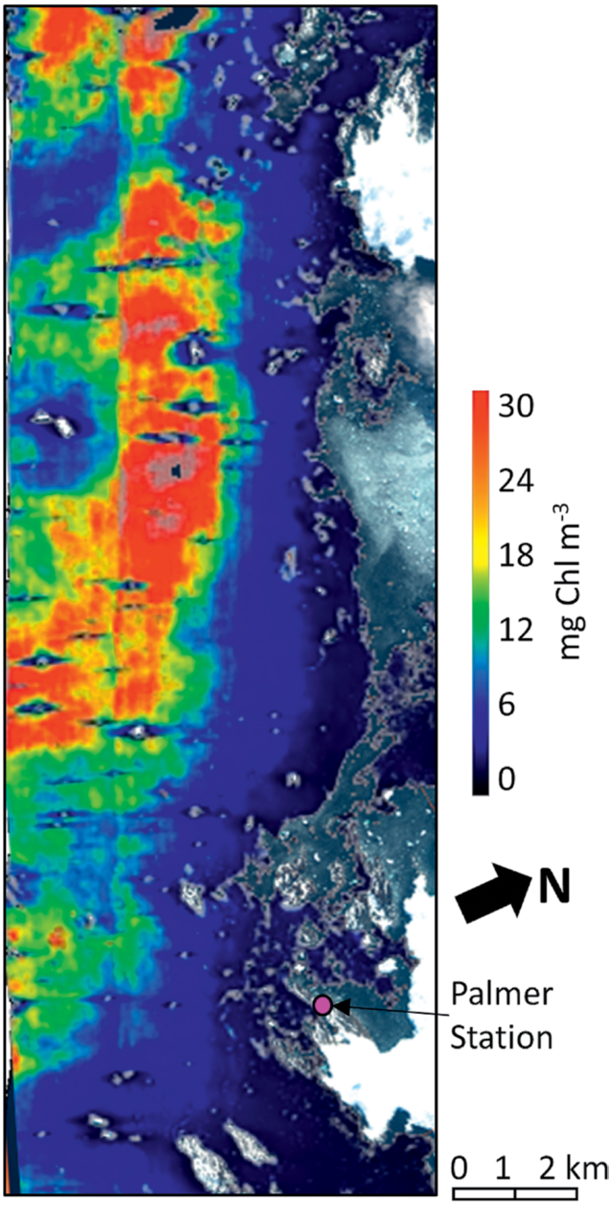

Fig. 12. High-resolution image of Palmer Station and vicinity from the PRISM sensor showing patchy distribution of phytoplankton chlorophyll a. A semianalytical inversion algorithm is being developed using spectra measured aboard the ARSV *L. M. Gould* in collaboration with the Palmer LTER.

It is also important to accurately represent ice supersaturation (ISS) in model simulations. Tan et al. (2016) showed that misrepresenting ISS conditions as cirrus clouds can lead to significant radiative forcing biases in a vertical column with an average of ~4.2 W m^{-2} increase in the net radiation at the top of the atmosphere. In addition, Diao et al. (2014) compared the distributions of clear-sky ISS conditions between the Northern and Southern Hemispheres and pointed out that more sampling in the Southern Hemisphere is needed to examine the relationship between the ISS occurrence frequency and aerosol concentration. Water vapor measurements from the ORCAS campaign provide a unique dataset to examine the distributions of ISS over the Southern Ocean. The occurrences of ISS for various temperature ranges are shown in Fig. 14. For the full campaign, ISS occurred ~2.3% and ~13.4% of the time at temperatures <−40° and from −40° to 0°C, respectively. The ISS conditions had a broad distribution across various latitudes and altitudes. The layer-normalized frequency of clear-sky ISS, in-cloud ISS, and non-ISS in-cloud conditions from the ORCAS data are shown in Fig. 14b. In preliminary comparisons of ORCAS data to CAM (version 5.3), the simulations underestimate the frequency of clear-sky ISS at −50° to 0°C by about 50% in relative difference, while the frequency of in-cloud ISS is overestimated in the model (J. D'Alessandro et al. 2017, unpublished manuscript).

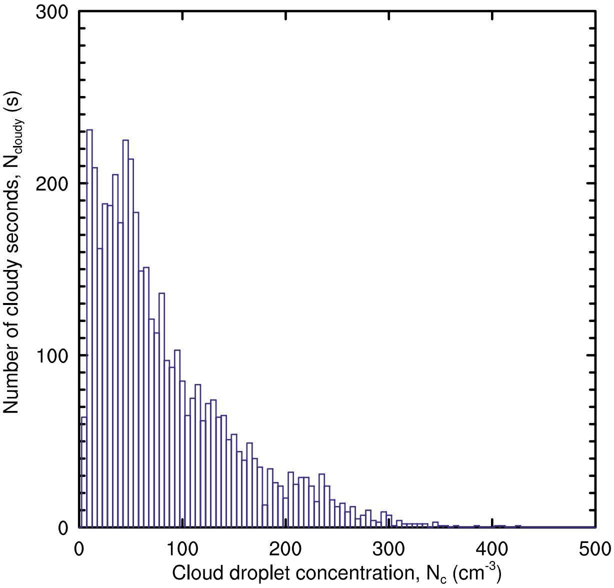

Fig. 13. Frequency distribution of cloud droplet concentration from the CDP during ORCAS. The measurements were mostly from marine stratocumulus, but some deeper clouds were also encountered. Only measurements from vertical soundings are included to ensure clouds were sampled evenly at all altitudes. The average cloud drop concentration is N_c = 84 cm^{-3}, for 4,421 one-second cloudy samples, with a pronounced tail toward higher values of N_c. A 1-s sample is considered cloudy if all ten 10-Hz subsamples have a droplet concentration higher than 5 cm^{-3}; this requirement is used to exclude partially cloudy samples.

SUMMARY. The ORCAS campaign succeeded in its goal of collecting measurements that can improve observational constraints on air–sea exchange of CO_2 and O_2 over the Southern Ocean. ORCAS collected an unprecedented set of continuous, flask-based, and remote sensing measurements at both high resolution and large spatial extent over a remote region that is biogeochemically and climatically important. The airborne measurements of atmospheric composition reflect processes operating on spatial scales from hundreds to thousands of kilometers and temporal scales from a day to several months and, hence, provide opportunities for testing understanding and model performance of a broad range of phenomena. At the largest spatial extent, these observations can help to quantify summertime Southern Ocean outgassing of O_2 and ingassing of CO_2, thus contributing to our understanding of the drivers of seasonal exchange rates. At smaller scales, the ORCAS measurements provide information on the spatial and temporal distribution of O_2 and CO_2 fluxes. The ratios between O_2 and CO_2 gradients observed in the atmosphere indicate a dominance of biological over thermal forcing of summertime CO_2 fluxes, which can provide a critical test for divergent Earth system models.

The large number of additional measurements carried out on the GV for ORCAS should also provide valuable insights across a wide range of ocean and atmosphere disciplines. For example, the non-CO_2 greenhouse gases and other industrial pollutants can clarify the long-range transport and anthropogenic influences contributing to observed CO_2 and O_2 distributions in the Southern Ocean. Furthermore, the spatial and temporal distributions of marine biogenic VOCs and their relationships to O_2 and CO_2 can support unique constraints on source processes. Hyperspectral ocean color measurements can be used to investigate the spatial distribution and productivity of calcite-producing organisms, as well as plankton speciation in regions of distinct biogenic emission plumes. Finally, the cloud microphysical measurements can contribute to resolving key uncertainties in the physical climate system and guide future observational efforts on Southern Ocean clouds.

While the Southern Ocean has historically been poorly sampled for biogeochemical and climate studies, recent investments and technological advances are changing this picture. The ORCAS campaign ran in parallel with the ongoing PALTER and DPT efforts on the *Gould* and coincident with the initial phases of a dramatic increase in tethered and float-based observations provided by the Ocean Observatories Initiative (OOI; http://oceanobservatories.org) and the Southern Ocean Carbon and Climate Observations and Modeling (SOCCOM; http://soccom.princeton.edu) project. Numerous synergies exist between our airborne measurements and those made by these projects on different time and space scales, and these will be exploited through collaborative analyses. Airborne O_2 measurements and intensive airborne biogeochemical sampling over the Southern Ocean are both new approaches. Thus, one of our primary objectives will be to quantify the utility of the data to understanding Southern Ocean biogeochemistry and how to design future observational campaigns. Earth system models will provide a key framework for synthesizing observations, developing process understanding, and planning future experiments. The ORCAS dataset, together with the related measurement efforts described above, will serve as a benchmark for models and will ultimately lead to improved understanding of Southern Ocean carbon–climate feedbacks.

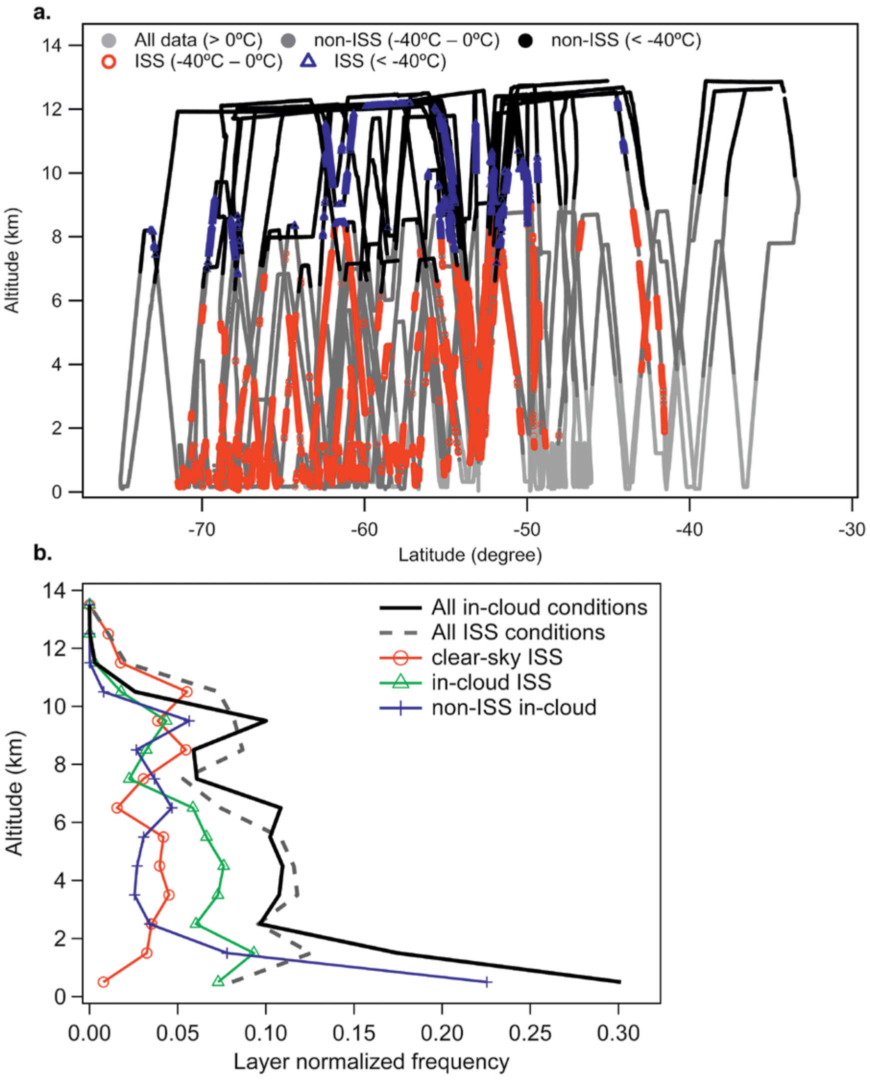

Fig. 14. (a) Altitudinal and latitudinal distribution of ISS conditions (red and blue markers) at various temperature ranges for the full campaign. (b) Layer-normalized frequency of three types of conditions: clear-sky ISS, in-cloud ISS, and non-ISS in-cloud conditions based on the ORCAS data. Relative humidity with respect to ice (RH_i) is calculated for temperatures below 0°C. Measurements by the VCSEL hygrometer and the Rosemount temperature probe are used in this calculation, with a combined uncertainty of ~6.3%–7.5% RH_i at 233.15–204.6 K, respectively. Note that between −40° and 0°C, the existence of supercooled liquid water likely leads to liquid water saturation, which corresponds to supersaturation with respect to ice.

ACKNOWLEDGMENTS.

The complete ORCAS dataset is publicly available (at www.eol.ucar.edu/field_projects/orcas). The GV operations, and QCLS, TOGA, AWAS, cloud microphysics, and state parameter instruments were supported by the NSF Lower Atmosphere Observing Facilities and NCAR Earth Observing Laboratory (EOL). We thank the NCAR Research Aviation Facility pilots, technicians, mechanics, and project managers for their excellent support, as well as additional NCAR EOL staff for assistance with project management, computing support, data archiving, and education and outreach activities. U.S. Antarctic Program staff provided additional logistic support. The ORCAS science activities are supported by NSF Polar Programs Grants 1501993, 1501997, 1501292, 1502301, and 1543457; NSF Atmospheric Chemistry Grant 1535364; NSF Atmospheric and Geospace Grant 1104642; and NASA Grant NNH14ZDA001N-RRNES. We would additionally like to thank the scientific and support staff of the Palmer Antarctica LTER (PALTER) program and ARSV *L. M. Gould*, and in particular

Hugh Ducklow, who collected additional flask samples for O_2 and CO_2 and supported measurements for remote sensing validation and algorithm development, as well as the Southern Ocean Carbon and Climate Observations and Modeling (SOCCOM) team for releasing several floats in the ORCAS domain and supporting ongoing collaborations. We thank Rich Lueb for engineering support of the AWAS sampling effort and Tim Newberger for engineering support of the NOAA–CU Picarro instrument. We are grateful to Alison Rockwell for organizing educational and outreach materials and activities. Tim Scheitlin prepared the CESM animation provided as a supplement. PRISM activities were carried out at the Jet Propulsion Laboratory, California Institute of Technology, under a contract with NASA. As part of the PRISM team, we would like to acknowledge P. Mouroulis, P. Sullivan, P. Kobzeff, L. Kroll, H. Luong, D. R. Thompson, B. Van Gorp, D. Keymeulen, J. Shaw, F. Loya, C. Sarture, M. Helmlinger, M. Hernandez, and S. Lundeen for technical assistance, operations, algorithm development, and data processing and management. M. Diao acknowledges funding from the NCAR Advanced Study Program Faculty Fellowship program. We would like to acknowledge high-performance computing support from Yellowstone (ark:/85065/d7wd3xhc) provided by NCAR's Computational and Information Systems Laboratory. The National Center for Atmospheric Research is sponsored by the National Science Foundation.

REFERENCES

Akima, H., 1978: A method of bivariate interpolation and smooth surface fitting for irregularly distributed data points. *ACM Trans. Math. Software*, **4**, 148–159, https://doi.org/10.1145/355780.355786.

Anav, A., and Coauthors, 2013: Evaluating the land and ocean components of the global carbon cycle in the CMIP5 Earth system models. *J. Climate*, **26**, 6801–6843, https://doi.org/10.1175/JCLI-D-12-00417.1.

Anderson, L. A., and J. L. Sarmiento, 1994: Redfield ratios of remineralization determined by nutrient data analysis. *Global Biogeochem. Cycles*, **8**, 65–80, https://doi.org/10.1029/93GB03318.

Andreae, M. O., and P. J. Crutzen, 1997: Atmospheric aerosols: Biogeochemical sources and role in atmospheric chemistry. *Science*, **276**, 1052–1058, https://doi.org/10.1126/science.276.5315.1052.

Andrews, S., and Coauthors, 2016: A comparison of very short lived halocarbon (VSLS) and DMS aircraft measurements in the tropical west Pacific from CAST, ATTREX and CONTRAST. *Atmos. Meas. Tech.*, **9**, 5213–5225, https://doi.org/10.5194/amt-9-5213-2016.

Apel, E. C., and Coauthors, 2015: Upper tropospheric ozone production from lightning NO_x-impacted convection: Smoke ingestion case study from the DC3 campaign. *J. Geophys. Res. Atmos.*, **120**, 2505–2523, https://doi.org/10.1002/2014JD022121.

Balch, W. M., D. T. Drapeau, B. C. Bowler, E. Lyczskowski, E. S. Booth, and D. Alley, 2011: The contribution of coccolithophores to the optical and inorganic carbon budgets during the Southern Ocean Gas Exchange Experiment: New evidence in support of the "Great Calcite Belt" hypothesis. *J. Geophys. Res.*, **116**, C00F06, https://doi.org/10.1029/2011JC006941.

Bent, J., 2014: Airborne oxygen measurements over the Southern Ocean as an integrated constraint of seasonal biogeochemical processes. Ph.D. dissertation, University of California, San Diego, 276 pp.

Boers, R., J. B. Jensen, P. B. Krummel, and H. Gerber, 1996: Microphysical and radiative structure of wintertime stratocumulus clouds over the Southern Ocean. *Quart. J. Roy. Meteor. Soc.*, **122**, 1307–1339, https://doi.org/10.1002/qj.49712253405.

Ceppi, P., Y.-T. Hwang, D. M. W. Frierson, and D. L. Hartmann, 2012: Southern Hemisphere jet latitude biases in CMIP5 models linked to shortwave cloud forcing. *Geophys. Res. Lett.*, **39**, L19708, https://doi.org/10.1029/2012GL053115.

——, M. D. Zelinka, and D. L. Hartmann, 2014: The response of the Southern Hemispheric eddy-driven jet to future changes in shortwave radiation in CMIP5. *Geophys. Res. Lett.*, **41**, 3244–3250, https://doi.org/10.1002/2014GL060043.

Chubb, T., Y. Huang, J. Jensen, T. Campos, S. Siems, and M. Manton, 2016: Observations of high droplet number concentrations in Southern Ocean boundary layer clouds. *Atmos. Chem. Phys.*, **16**, 971–987, https://doi.org/10.5194/acp-16-971-2016.

de Gouw, J. A., C. Warneke, D. D. Parrish, J. S. Holloway, M. Trainer, and F. C. Fehsenfeld, 2003: Emission sources and ocean uptake of acetonitrile (CH_3CN) in the atmosphere. *J. Geophys. Res.*, **108**, 4329, https://doi.org/10.1029/2002JD002897.

Diao, M., M. A. Zondlo, A. J. Heymsfield, and S. P. Beaton, 2014: Hemispheric comparison of cirrus cloud evolution using in situ measurements in HIAPER pole-to-pole observations. *Geophys. Res. Lett.*, **41**, 4090–4099, https://doi.org/10.1002/2014GL059873.

Dierssen, H. M., R. C. Smith, and M. Vernet, 2002: Glacial meltwater dynamics in coastal waters west of the Antarctic Peninsula. *Proc. Natl. Acad. Sci. USA*, **99**, 1790–1795, https://doi.org/10.1073/pnas.032206999.

Dorsi, S. W., L. E. Kalnajs, D. W. Toohey, and L. M. Avallone, 2014: A fiber-coupled laser hygrometer for airborne total water measurement. *Atmos. Meas. Tech.*, **7**, 215–223, https://doi.org/10.5194/amt-7-215-2014.

Downes, S. M., and Coauthors, 2015: An assessment of Southern Ocean water masses and sea ice during 1988–2007 in a suite of interannual CORE-II simulations. *Ocean Modell.*, **94**, 67–94, https://doi.org/10.1016/j.ocemod.2015.07.022.

Fischer, E. V., D. J. Jacob, D. B. Millet, R. M. Yantosca, and J. Mao, 2012: The role of the ocean in the global atmospheric budget of acetone. *Geophys. Res. Lett.*, **39**, L01807, https://doi.org/10.1029/2011GL050086.

Flocke, F., and Coauthors, 1999: An examination of chemistry and transport processes in the tropical lower stratosphere using observations of long-lived and short-lived compounds obtained during STRAT and POLARIS. *J. Geophys. Res.*, **104**, 26 625–26 642, https://doi.org/10.1029/1999JD900504.

Gille, S., 2008: Decadal-scale temperature trends in the Southern Hemisphere ocean. *J. Climate*, **21**, 4749–4765, https://doi.org/10.1175/2008JCLI2131.1.

Goodwin, K. D., W. J. North, and M. E. Lidstrom, 1997: Production of bromoform and dibromomethane by giant kelp: Factors affecting release and comparison to anthropogenic bromine sources. *Limnol. Oceanogr.*, **42**, 1725–1734, https://doi.org/10.4319/lo.1997.42.8.1725.

Hogg, A. M., M. P. Meredith, D. P. Chambers, E. P. Abrahamsen, C. W. Hughes, and A. K. Morrison, 2015: Recent trends in the Southern Ocean eddy field. *J. Geophys. Res. Oceans*, **120**, 257–267, https://doi.org/10.1002/2014JC010470.

Holzer, M., and D. W. Waugh, 2015: Interhemispheric transit time distributions and path-dependent lifetimes constrained by measurements of SF_6, CFCs, and CFC replacements. *Geophys. Res. Lett.*, **42**, 4581–4589, https://doi.org/10.1002/2015GL064172.

Hurrell, J. W., and Coauthors, 2013: The Community Earth System Model: A framework for collaborative research. *Bull. Amer. Meteor. Soc.*, **94**, 1339–1360, https://doi.org/10.1175/BAMS-D-12-00121.1.

Ito, T., A. Bracco, C. Deutsch, H. Frenzel, M. C. Long, and Y. Takano, 2015: Sustained growth of the Southern Ocean carbon storage in a warming climate. *Geophys. Res. Lett.*, **42**, 4516–4522, https://doi.org/10.1002/2015GL064320.

Jiang, C., S. T. Gille, J. Sprintall, and C. Sweeney, 2014: Drake Passage oceanic $p\mathrm{CO}_2$: Evaluating CMIP5 coupled carbon–climate models using in situ observations. *J. Climate*, **27**, 76–100, https://doi.org/10.1175/JCLI-D-12-00571.1.

Karion, A., and Coauthors, 2013: Long-term greenhouse gas measurements from aircraft. *Atmos. Meas. Tech.*, **6**, 511–526, https://doi.org/10.5194/amt-6-511-2013.

Keeling, R. F., A. C. Manning, E. M. McEvoy, and S. R. Shertz, 1998: Methods for measuring changes in atmospheric O_2 concentration and their application in Southern Hemisphere air. *J. Geophys. Res.*, **103**, 3381–3397, https://doi.org/10.1029/97JD02537.

Keene, W. C., and Coauthors, 1999: Composite global emissions of reactive chlorine from anthropogenic and natural sources: Reactive chlorine emissions inventory. *J. Geophys. Res.*, **104**, 8429–8440, https://doi.org/10.1029/1998JD100084.

Khalil, M., and R. Rasmussen, 1999: Atmospheric chloroform. *Atmos. Environ.*, **33**, 1151–1158, https://doi.org/10.1016/S1352-2310(98)00233-7.

Khatiwala, S., F. Primeau, and T. Hall, 2009: Reconstruction of the history of anthropogenic CO_2 concentrations in the ocean. *Nature*, **462**, 346–349, https://doi.org/10.1038/nature08526.

Landschutzer, P., and Coauthors, 2015: The reinvigoration of the Southern Ocean carbon sink. *Science*, **349**, 1221–1224, https://doi.org/10.1126/science.aab2620.

Le Quéré, C., and Coauthors, 2007: Saturation of the Southern Ocean CO_2 sink due to recent climate change. *Science*, **316**, 1735, https://doi.org/10.1126/science.1136188.

Lin, J., C. Gerbig, S. Wofsy, A. Andrews, B. Daube, K. Davis, and C. Grainger, 2003: A near-field tool for simulating the upstream influence of atmospheric observations: The Stochastic Time-Inverted Lagrangian Transport (STILT) model. *J. Geophys. Res.*, **108**, 4493, https://doi.org/10.1029/2002JD003161.

Lovenduski, N. S., and G. B. Bonan, 2017: Reducing uncertainty in projections of terrestrial carbon uptake. *Environ. Res. Lett.*, **12**, 044020, https://doi.org/10.1088/1748-9326/aa66b8.

Marandino, C. A., W. J. De Bruyn, S. D. Miller, M. J. Prather, and E. S. Saltzman, 2005: Oceanic uptake and the global atmospheric acetone budget. *Geophys. Res. Lett.*, **32**, L15806, https://doi.org/10.1029/2005GL023285.

Mayewski, P. A., and Coauthors, 2009: State of the Antarctic and Southern Ocean climate system. *Rev. Geophys.*, **47**, RG1003, https://doi.org/10.1029/2007RG000231.

McCulloch, A., M. L. Aucott, T. E. Graedel, G. Kleiman, P. M. Midgley, and Y.-F. Li, 1999: Industrial emissions of trichloroethene, tetrachloroethene, and dichloromethane: Reactive chlorine emissions inventory. *J. Geophys. Res.*, **104**, 8417–8427, https://doi.org/10.1029/1999JD900011.

Montzka, S. A., and Coauthors, 2011: Ozone-depleting substances (ODSs) and related chemicals. World Meteorological Organization Global Ozone Research and Monitoring Project Rep. 52, 1.1–1.108.

Moore, J. K., K. Lindsay, S. C. Doney, M. C. Long, and K. Misumi, 2013: Marine ecosystem dynamics and biogeochemical cycling in the Community Earth System Model [CESM1 (BGC)]: Comparison of the 1990s with the 2090s under the RCP4.5 and RCP8.5 scenarios. *J. Climate*, **26**, 9291–9312, https://doi.org/10.1175/JCLI-D-12-00566.1.

Mouroulis, P., and Coauthors, 2014: Portable Remote Imaging Spectrometer coastal ocean sensor: Design, characteristics, and first flight results. *Appl. Opt.*, **53**, 1363–1380, https://doi.org/10.1364/AO.53.001363.

Munro, D. R., N. S. Lovenduski, T. Takahashi, B. B. Stephens, T. Newberger, and C. Sweeney, 2015: Recent evidence for a strengthening CO_2 sink in the Southern Ocean from carbonate system measurements in the Drake Passage (2002–2015). *Geophys. Res. Lett.*, **42**, 7623–7630, https://doi.org/10.1002/2015GL065194.

Naud, C. M., D. J. Posselt, and S. C. van den Heever, 2012: Observational analysis of cloud and precipitation in midlatitude cyclones: Northern versus Southern Hemisphere warm fronts. *J. Climate*, **25**, 5135–5151, https://doi.org/10.1175/JCLI-D-11-00569.1.

Pan, L. L., and Coauthors, 2016: The Convective Transport of Active Species in the Tropics (CONTRAST) experiment. *Bull. Amer. Meteor. Soc.*, **98**, 106–128, https://doi.org/10.1175/BAMS-D-14-00272.1.

Pohl, B., N. Fauchereau, C. J. C. Reason, and M. Rouault, 2010: Relationships between the Antarctic Oscillation, the Madden–Julian oscillation, and ENSO, and consequences for rainfall analysis. *J. Climate*, **23**, 238–254, https://doi.org/10.1175/2009JCLI2443.1.

Powers, J. G., K. W. Manning, D. H. Bromwich, J. J. Cassano, and A. M. Cayette, 2012: A decade of Antarctic science support through AMPS. *Bull. Amer. Meteor. Soc.*, **93**, 1699–1712, https://doi.org/10.1175/BAMS-D-11-00186.1.

Purkey, S. G., and G. C. Johnson, 2010: Warming of global abyssal and deep Southern Ocean waters between the 1990s and 2000s: Contributions to global heat and sea level rise budgets. *J. Climate*, **23**, 6336–6351, https://doi.org/10.1175/2010JCLI3682.1.

Rienecker, M., and Coauthors, 2008: The GEOS-5 data assimilation system—Documentation of versions 5.0.1, 5.1.0, and 5.2.0. NASA Tech. Rep. Series on Global Modeling and Data Assimilation NASA/TM–2008–104606, Vol. 27, 118 pp.

Santoni, G. W., and Coauthors, 2014: Evaluation of the airborne quantum cascade laser spectrometer (QCLS) measurements of the carbon and greenhouse gas suite—CO_2, CH_4, N_2O, and CO—during the CalNex and HIPPO campaigns. *Atmos. Meas. Tech.*, **7**, 1509–1526, https://doi.org/10.5194/amt-7-1509-2014.

Schauffler, S., E. Atlas, D. Blake, F. Flocke, R. Lueb, J. Lee-Taylor, V. Stroud, and W. Travnicek, 1999: Distributions of brominated organic compounds in the troposphere and lower stratosphere. *J. Geophys. Res.*, **104**, 21 513–21 535, https://doi.org/10.1029/1999JD900197.

Simmonds, P. G., and Coauthors, 2006: Global trends, seasonal cycles, and European emissions of dichloromethane, trichloroethene, and tetrachloroethene from the AGAGE observations at Mace Head, Ireland, and Cape Grim, Tasmania. *J. Geophys. Res.*, **111**, D18304, https://doi.org/10.1029/2006JD007082.

Singh, H. B., and Coauthors, 2003: In situ measurements of HCN and CH_3CN over the Pacific Ocean: Sources, sinks, and budgets. *J. Geophys. Res.*, **108**, 8795, https://doi.org/10.1029/2002JD003006.

Skamarock, W. C., and Coauthors, 2008: A description of the Advanced Research WRF version 3. NCAR Tech. Note NCAR/TN-475+STR, 122 pp., https://doi.org/10.5065/D68S4MVH.

Stein, A. F., R. R. Draxler, G. D. Rolph, B. J. B. Stunder, M. D. Cohen, and F. Ngan, 2015: NOAA's HYSPLIT atmospheric transport and dispersion modeling system. *Bull. Amer. Meteor. Soc.*, **96**, 2059–2077, https://doi.org/10.1175/BAMS-D-14-00110.1.

Steinbach, J., C. Gerbig, C. Rödenbeck, U. Karstens, C. Minejima, and H. Mukai, 2011: The CO_2 Release and Oxygen Uptake from Fossil Fuel Emission Estimate (COFFEE) dataset: Effects from varying oxidative ratios. *Atmos. Chem. Phys.*, **11**, 6855–6870, https://doi.org/10.5194/acp-11-6855-2011.

Stephens, B. B., R. F. Keeling, M. Heimann, K. D. Six, R. Murnane, and K. Caldeira, 1998: Testing global ocean carbon cycle models using measurements of atmospheric O_2 and CO_2 concentration. *Global Biogeochem. Cycles*, **12**, 213–230, https://doi.org/10.1029/97GB03500.

——, ——, and W. J. Paplawsky, 2003: Shipboard measurements of atmospheric oxygen using a vacuum- ultraviolet absorption technique. *Tellus*, **55B**, 857–878, https://doi.org/10.1046/j.1435-6935.2003.00075.x.

Tagliabue, A., J.-B. Sallée, A. R. Bowie, M. Lévy, S. Swart, and P. W. Boyd, 2014: Surface-water iron supplies in the Southern Ocean sustained by deep winter mixing. *Nat. Geosci.*, **7**, 314–320, https://doi.org/10.1038/ngeo2101.

Talley, L. D., and Coauthors, 2016: Changes in ocean heat, carbon content, and ventilation: A review of the first decade of GO-SHIP global repeat hydrography. *Annu. Rev. Mar. Sci.*, **8**, 185–215, https://doi.org/10.1146/annurev-marine-052915-100829.

Tan, X., Y. Huang, M. Diao, A. Bansemer, M. Zondlo, J. DiGangi, R. Volkamer, and Y. Hu, 2016: An assessment of the radiative effects of ice supersaturation based on in situ observations. *Geophys. Res. Lett.*, **43**, 11 039–11 047, https://doi.org/10.1002/2016GL071144.

Thompson, D. W. J., and J. M. Wallace, 2000: Annular modes in the extratropical circulation. Part I: Month-to-month variability. *J. Climate*, **13**, 1000–1016, https://doi.org/10.1175/1520-0442(2000)013<1000:AMITEC>2.0.CO;2.

Trenberth, K. E., and J. T. Fasullo, 2010: Simulation of present-day and twenty-first-century energy budgets of the Southern Oceans. *J. Climate*, **23**, 440–454, https://doi.org/10.1175/2009JCLI3152.1.

Volkamer, R., and Coauthors, 2015: Aircraft measurements of BrO, IO, glyoxal, NO$_2$, H$_2$O, O$_2$–O$_2$ and aerosol extinction profiles in the tropics: Comparison with aircraft-/ship-based in situ and lidar measurements. *Atmos. Meas. Tech.*, **8**, 2121–2148, https://doi.org/10.5194/amt-8-2121-2015.

Wood, R., and Coauthors, 2011: The VAMOS Ocean-Cloud-Atmosphere-Land Study Regional Experiment (VOCALS-Rex): Goals, platforms and field operations. *Atmos. Chem. Phys.*, **11**, 627–654, https://doi.org/10.5194/acp-11-627-2011.

Zondlo, M. A., M. E. Paige, S. M. Massick, and J. A. Silver, 2010: Vertical cavity laser hygrometer for the National Science Foundation Gulfstream-V aircraft. *J. Geophys. Res.*, **115**, D20309, https://doi.org/10.1029/2010JD014445.